Astronomy & Astrophysics

The Carnegie Supernova Project II

Observations of the luminous red nova AT 2014ej[★,★★]

M. D. Stritzinger[1], F. Taddia[1], M. Fraser[2], T. M. Tauris[3,1], C. Contreras[1,4], S. Drybye[1,5], L. Galbany[6], S. Holmbo[1], N. Morrell[4], A. Pastorello[7], M. M. Phillips[4], G. Pignata[8,9], L. Tartaglia[10], N. B. Suntzeff[11,12], J. Anais[4], C. Ashall[13], E. Baron[14], C. R. Burns[15], P. Hoeflich[13], E. Y. Hsiao[13], E. Karamehmetoglu[1], T. J. Moriya[16,17], G. Bock[18], A. Campillay[4], S. Castellón[4], C. Inserra[19], C. González[4], P. Marples[20], S. Parker[21], D. Reichart[22], S. Torres-Robledo[23,4], and D. R. Young[24]

[1] Department of Physics and Astronomy, Aarhus University, Ny Munkegade 120, 8000 Aarhus C, Denmark
 e-mail: `max@phys.au.dk`
[2] School of Physics, O'Brien Centre for Science North, University College Dublin, Belfield, Dublin 4, Ireland
[3] Aarhus Institute of Advanced Studies (AIAS), Aarhus University, Høegh-Guldbergs Gade 6B, 8000 Aarhus C, Denmark
[4] Las Campanas Observatory, Carnegie Observatories, Casilla 601, La Serena, Chile
[5] Nordic Optical Telescope, Apartado 474, 38700 Santa Cruz de La Palma, Spain
[6] Departamento de Física Teórica y del Cosmos, Universidad de Granada, 18071 Granada, Spain
[7] INAF – Osservatorio Astronomico di Padova, Vicolo dell'Osservatorio 5, 35122 Padova, Italy
[8] Departamento de Ciencias Fisicas, Universidad Andres Bello, Avda. Republica 252, Santiago, Chile
[9] Millennium Institute of Astrophysics, Santiago, Chile
[10] The Oskar Klein Centre, Department of Astronomy, Stockholm University, AlbaNova 10691, Stockholm, Sweden
[11] The George P. and Cynthia Woods Mitchell Institute for Fundamental Physics and Astronomy, Texas A&M University, College Station, TX 877843, USA
[12] Department of Physics and Astronomy, Texas A&M University, College Station, TX 77843, USA
[13] Department of Physics, Florida State University, Tallahassee, FL 32306, USA
[14] Homer L. Dodge Department of Physics and Astronomy, University of Oklahoma, 440 W. Brooks, Rm 100, Norman, OK 73019-2061, USA
[15] Observatories of the Carnegie Institution for Science, 813 Santa Barbara St, Pasadena, CA 91101, USA
[16] National Astronomical Observatory of Japan, National Institutes of Natural Sciences, 2-21-1 Osawa, Mitaka, Tokyo 181-8588, Japan
[17] School of Physics and Astronomy, Faculty of Science, Monash University, Clayton, VIC 3800, Australia
[18] Runaway Bay, Gold Coast, Queensland, Australia
[19] School of Physics & Astronomy, Cardiff University, Queens Buildings, The Parade, Cardiff CF24 3AA, UK
[20] Leyburn Observatory, Queensland 4129, Australia
[21] Parkdales Observatory, Oxford, New Zealand
[22] University of North Carolina at Chapel Hill, Campus Box 3255, Chapel Hill, NC 27599-3255, USA
[23] SOAR Telescope, La Serena 1700000, Chile
[24] Astrophysics Research Centre, School of Mathematics and Physics, Queen's University Belfast, Belfast BT7 1NN, UK

ABSTRACT

We present optical and near-infrared broadband photometry and optical spectra of AT 2014ej from the Carnegie Supernova Project-II. These observations are complemented with data from the CHilean Automatic Supernova sEarch, the Public ESO Spectroscopic Survey of Transient Objects, and from the Backyard Observatory Supernova Search. Observational signatures of AT 2014ej reveal that it is similar to other members of the gap-transient subclass known as luminous red novae (LRNe), including the ubiquitous double-hump light curve and spectral properties similar to that of LRN SN 2017jfs. A medium-dispersion visual-wavelength spectrum of AT 2014ej taken with the *Magellan Clay* telescope exhibits a P Cygni Hα feature characterized by a blue velocity at zero intensity of $\approx 110\,\mathrm{km\,s^{-1}}$ and a P Cygni minimum velocity of $\approx 70\,\mathrm{km\,s^{-1}}$. We attribute this to emission from a circumstellar wind. Inspection of pre-outbust *Hubble* Space Telescope images yields no conclusive progenitor detection. In comparison with a sample of LRNe from the literature, AT 2014ej lies at the brighter end of the luminosity distribution. Comparison of the ultra-violet, optical, infrared light curves of well-observed LRNe to common-envelope evolution models from the literature indicates that the models underpredict the luminosity of the comparison sample at all phases and also produce inconsistent timescales of the secondary peak. Future efforts to model LRNe should expand upon the current parameter space we explore here and therefore may consider more massive systems and a wider range of dynamical timescales.

Key words. supernovae: individual: AT2014ej – supernovae: general

---

[★] This paper includes data gathered with the 6.5 meter *Magellan* telescopes at Las Campanas Observatory, Chile.
[★★] Photometry and spectra are presented in this paper are available on WISeREP.

1. Introduction

This is the second of two papers by the Carnegie Supernova Project-II (CSP-II) that each present a case study of a gap transient. Gap transients are located within the so-called "luminosity gap" parameter space that is devoid of bright novae ($M_V \lesssim -10$ mag) and the least luminous core-collapse supernovae (SN; peak $M_V \sim -16$ mag). Because the visual wavelength spectra of gap transients (in the past also often referred to as intermediate luminosity optical transients) typically resemble the spectra of interacting type IIn SNe, they were historically commonly called SN imposters (e.g., Schlegel 1990; Filippenko 1997; Van Dyk et al. 2000). As the population of gap transients with decent observational data has increased, it has become apparent that the diversity displayed among the literature sample suggests distinctly different populations (see Kulkarni & Kasliwal 2009; Kochanek et al. 2012a; Kashi & Soker 2016; Pastorello & Fraser 2019, for more detailed discussion).

Today, at least three known populations of gap transients are recognized in the luminoisty gap. These include classical luminous blue variable (LBV) outbursts, intermediate-luminosity red transients (ILRTs), and luminous red novae (LRNe). LBVs are thought to be related to eruptions of massive luminous stars (see Smith et al. 2011). As shown in greater detail in Stritzinger et al. (2020, hereafter Paper I), the ILRT subtype is well represented by NGC 300-2008-OT and SN 2008S, and has been linked to asymptotic giant branch (S-AGB) stars (Prieto et al. 2008, 2009; Thompson et al. 2009; Botticella et al. 2009; Kochanek 2011; Adams et al. 2016; Doherty et al. 2017) that die as electron-capture supernovae (Miyaji et al. 1980; Nomoto 1984; Miyaji & Nomoto 1987; Hashimoto et al. 1993; Kitaura et al. 2006; Poelarends et al. 2008). Other models appearing in the literature for ILRTs consist of moderately massive stars experiencing super-Eddington winds and/or giant outbursts (e.g., Smith et al. 2009; Humphreys et al. 2011), or massive stars donating material to a main-sequence star, leading to the release of gravitational energy (e.g., Kashi et al. 2010). Finally, a leading model for the origins of LRNe, which all display a ubiquitous double-humped light curve (Pastorello et al. 2019a), consists of the ejection of a common envelope by a massive binary system (e.g., Blagorodnova et al. 2017) upon coalescence (Smith et al. 2016; Metzger & Pejcha 2017; Lipunov et al. 2017; Mauerhan et al. 2018). However, other models have also been proposed in the past to account for LRNe, particularly within articles that have studied the Galactic LRN archetype V838 Mon. These include, among others, outbursts from massive stars (Tylenda 2005), accretion of low-mass stars onto solar-mass main-sequence companions (Soker & Tylenda 2003; Tylenda & Soker 2006; Kashi et al. 2010; Kashi & Soker 2016; Soker 2020), or even giant stars that accrete relatively massive planets (Retter & Marom 2003).

The locations of the three gap-transient subtypes in the luminosity versus decay time (defined as the time interval in which the r-band light curve drops one magnitude from peak) parameter space are shown in Fig. 1 of Paper I. In general, the various gap-transient subtypes exhibit similar peak luminosities, while differences among their light curve decay times are apparent. LBVs tend to exhibit a more slowly declining light-curve evolution. For example, as indicated in Fig. 1 of Paper I, LBVs typically exhibit decay timescales of $\gtrsim 10^2$ days. On the other hand, both ILRTs and LRNe typically decay on shorter timescales of $10^1 - 10^2$ days. Because very few gap transients have been studied in depth, the full extent of the peak luminosity versus decay
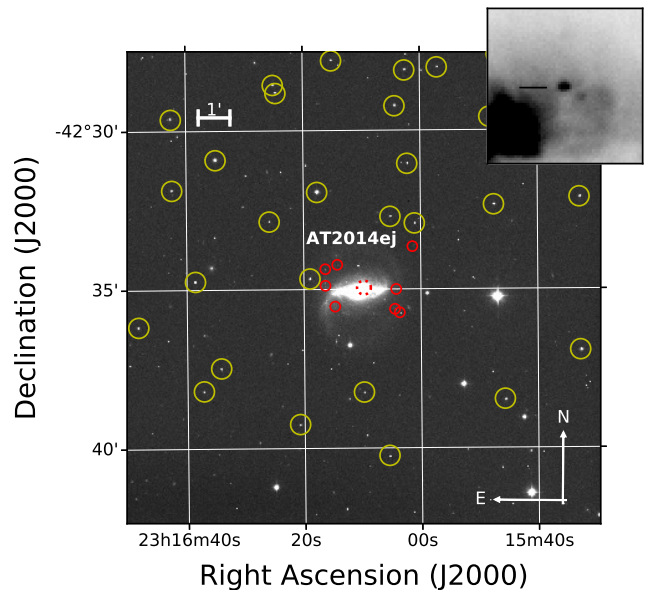

Fig. 1. Finding chart of NGC 7552 hosting AT 2014ej constructed from a single Swope r-band image. The position of the transient is indicated with a dotted circle with a zoom-in of the area enclosed shown in the upper right corner inset. Optical and NIR local sequence stars are indicated with yellow and red circles, respectively.

time parameter space populated by both ILRTs and LRNe is currently unknown.

Similar to the ILRT SNhunt120 presented in Paper I, here in Paper II, we add to the small but growing sample of LRNe with our observational data set of AT 2014ej. The data set is based largely on observations performed by the CSP-II (Phillips et al. 2019). This includes optical light curves and some near-IR (NIR) photometry, as well as one low- and one medium-dispersion visual wavelength spectrum. The CSP-II data are clearly complemented with unfiltered images from the Backyard Observatory Supernova Search[1] (BOSS) and the CHilean Automatic Supernova sEarch (CHASE; Reichart et al. 2005), as well as a handful of visual wavelength spectra and optical/NIR broadband photometric measurements obtained by the Public ESO Spectroscopic Survey of Transient Objects (PESSTO; Smartt et al. 2015). In addition, archival images of the host galaxy NGC 7552 obtained with the *Hubble* Space Telescope (HST) are examined in order to compute progenitor limits.

2. AT 2014ej

2.1. Discovery, distance, and reddening

PSN J23160979−4234575 (hereafter we refer to this transient by its Transient Name Server designation AT 2014ej) was discovered in NGC 7552 on 2014 September 24.46 UT by Peter Marples during the course of the BOSS (Bock et al. 2014) and was confirmed to be ~17.8 ± 0.4 magnitude in unfiltered image taken by G. Bock on 2014 September 24.5 UT. Bock et al. also reported nondetections from images with a limiting magnitude of ~18.5 taken on 2.46 and 2014 September 10.50 2014 UT. We reexamined the discovery image, and after removing the host at the position of the transient, we computed photometry relative to r-band photometry of a local sequence of stars in the field of NGC 7552 (see Sect. 2.2). This provides an apparent magnitude

---

[1] https://www.bosssupernova.com/

Table 1. Optical photometry of the local sequence for AT 2014ej in the "standard" system.

ID	α(2000)	δ(2000)	B	V	u'	g'	r'	i'
1	349.073883	−42.532539	. . .	. . .	. . .	. . .	. . .	. . .
2	349.146027	−42.515438	. . .	. . .	. . .	. . .	. . .	. . .
3	348.886597	−42.615513	14.807(010)	14.145(007)	15.940(034)	14.434(007)	13.949(005)	13.805(007)
4	349.104828	−42.476219	15.332(013)	14.847(011)	16.056(036)	15.053(009)	14.713(007)	14.605(011)
5	348.940552	−42.641197	15.983(037)	15.050(030)	17.578(091)	15.504(031)	14.689(029)	14.316(014)
6	349.160797	−42.579163	15.729(022)	15.144(010)	16.608(051)	15.402(011)	14.974(008)	14.828(007)
7	349.018341	−42.487396	15.825(007)	15.114(011)	16.957(050)	15.434(012)	14.883(008)	14.683(010)
8	349.177582	−42.494061	16.206(039)	15.209(009)	18.097(048)	15.689(015)	14.782(010)	14.447(009)
9	349.201538	−42.602962	15.843(024)	15.269(010)	16.636(050)	15.515(009)	15.114(009)	14.967(011)
10	348.887085	−42.535305	16.070(021)	15.241(010)	17.454(089)	15.626(013)	14.936(008)	14.675(008)
11	349.011200	−42.468658	15.985(017)	15.422(008)	16.833(051)	15.671(012)	15.273(011)	15.141(012)
12	348.950928	−42.493233	16.349(015)	15.528(011)	17.800(063)	15.903(011)	15.248(013)	15.027(011)
13	349.079193	−42.577908	16.528(029)	15.614(012)	17.847(229)	16.049(013)	15.289(008)	14.948(010)
14	348.948059	−42.539196	16.196(030)	15.621(013)	17.028(082)	15.875(015)	15.465(016)	15.316(011)
15	349.177124	−42.531296	16.463(027)	15.645(015)	17.914(059)	16.018(015)	15.356(012)	15.141(009)
16	349.107941	−42.547867	16.849(022)	16.196(028)	17.786(073)	16.488(034)	15.999(016)	15.842(022)
17	349.041046	−42.637428	18.129(070)	17.004(051)	19.990(061)	17.570(043)	16.477(030)	16.051(021)
18	349.142731	−42.624664	17.243(031)	16.379(035)	18.671(075)	16.785(021)	16.065(016)	15.824(018)
19	349.086792	−42.654221	17.109(047)	16.521(032)	17.911(083)	16.773(014)	16.358(019)	16.216(036)
20	349.004547	−42.548927	17.406(080)	16.513(033)	18.663(085)	16.931(037)	16.227(014)	15.914(024)
21	349.021851	−42.545380	17.152(040)	16.558(030)	17.871(092)	16.843(046)	16.377(019)	16.174(017)
22	349.063202	−42.463596	17.234(067)	16.593(036)	18.179(051)	16.868(033)	16.405(032)	16.243(030)
23	349.155212	−42.636612	17.182(050)	16.607(023)	17.946(056)	16.847(031)	16.477(013)	16.358(019)
24	348.945343	−42.460548	17.043(035)	16.618(040)	17.523(170)	16.811(024)	16.502(037)	16.415(061)
25	349.102997	−42.480492	17.794(058)	16.606(041)	19.879(052)	17.199(042)	16.088(015)	15.623(015)
26	349.023193	−42.670746	17.517(080)	16.726(046)	18.875(074)	17.077(049)	16.433(016)	16.205(022)
27	349.009583	−42.517628	17.768(078)	16.937(036)	19.021(070)	17.327(021)	16.621(039)	16.345(027)
28	348.988068	−42.467167	17.582(100)	16.962(035)	18.510(044)	17.236(044)	16.762(023)	16.626(037)

Notes. Values in parenthesis are 1-σ uncertainties that correspond to the rms of the instrumental errors of the photometry obtained over a minimum of three nights observed relative to standard star fields.

Table 2. NIR photometry of the local sequences for AT 2014ej in the "standard" system.

ID	α(2000)	δ(2000)	Y	N	J_{rc2}	N	H	N
101	349.044870	−42.571004	15.64(02)	3	15.38(04)	3	15.07(07)	3
102	349.018801	−42.593902	16.57(06)	3	16.11(06)	3	15.61(16)	3
103	349.015365	−42.595754	17.60(07)	2	. . .	. . .	. . .	. . .
104	349.061355	−42.592496	17.52(41)	2	17.08(21)	3	17.01(15)	1
106	349.068255	−42.572860	18.37(11)	1	. . .	. . .	. . .	. . .
107	349.059690	−42.570588	18.29(10)	1	. . .	. . .	. . .	. . .
109	349.006081	−42.561110	18.54(12)	1	. . .	. . .	. . .	. . .

Notes. Uncertainties given in parentheses in thousandths of a magnitude correspond to an rms of the magnitudes obtained on photometric nights.

of 17.96 ± 0.11 mag on 2014 September 24 (MJD 56923.66), which is slightly fainter than the value reported (Bock et al. 2014). Furthermore, we compute a 3-sigma nondetection limit of 17.8 mag for an image obtained by BOSS on the previous night.

As shown below, AT 2014ej was recovered in unfiltered search images taken by CHASE about four days prior to the BOSS detection on 2014 September 20.06 with an apparent magnitude of 17.5 ± 0.1. The J2000 coordinates of AT 2014ej are $\alpha = 23^h16^m09\overset{s}{.}79$ and $\delta = -42°34'57\overset{''}{.}5$, which is 10″.9 west and 7″.6 north from the core of its SBab host galaxy NGC 7552. A finding chart of NGC 7552 is shown in Fig. 1.

Morrell et al. (2014) obtained a visual wavelength spectrum with the du Pont telescope located at the Las Campanas Observatory (LCO) on 2014 September 27.2 UT and classified AT 2014ej as a SN imposter. This early spectrum exhibits Balmer line velocities of ≈800 km s^{-1}. As the transient appeared to be caught on the rise, the CSP-II decided to include it within its followup program.

According to NED, NGC 7552 is located at a heliocentric redshift of $z = 0.00537 \pm 0.00002$ (1608 km s^{-1}). To convert this redshift into distance, we adopted the following cosmological parameters: $H_0 = 73.2 \pm 2.3$ km s^{-1} Mpc^{-1} (Burns et al. 2018), $\Omega_m = 0.27$, and $\Omega_L = 0.73$, as well as a correction from NED based on Virgo, Great Attractor, and Shapley in-flow models. According to this, the redshift distance corresponds to a distance modulus of $\mu = 31.72 \pm 0.15$ mag and hence the distance $D = 22.07 \pm 1.53$ Mpc.

Table 3. Optical photometry of AT 2014ej in the Swope "natural" system.

Time [a]	u	Time [a]	B	Time [a]	g	Time [a]	V	Time [a]	r	Time [a]	i
$\cdots$	$\cdots$	25.71	18.472(0.038)	25.70	18.178(0.033)	25.71	18.022(0.035)	25.70	17.739(0.035)	25.71	17.702(0.037)
26.64	19.226(0.040)	26.62	18.556(0.035)	26.63	18.297(0.034)	26.63	18.085(0.037)	26.63	17.829(0.031)	26.63	17.801(0.029)
27.62	19.322(0.036)	27.63	18.619(0.037)	27.61	18.402(0.045)	27.63	18.201(0.037)	27.61	17.962(0.037)	27.62	17.985(0.034)
28.62	19.468(0.050)	28.61	18.737(0.036)	28.61	18.542(0.035)	28.61	18.266(0.043)	28.61	18.023(0.029)	28.61	17.953(0.032)
29.61	19.509(0.048)	29.62	18.835(0.032)	29.59	18.544(0.061)	29.62	18.372(0.044)	29.60	18.144(0.037)	29.60	18.073(0.024)
30.59	19.586(0.034)	30.61	18.900(0.033)	30.60	18.604(0.032)	30.61	18.387(0.033)	30.59	18.190(0.034)	30.60	18.088(0.035)
31.64	19.753(0.052)	31.63	19.012(0.043)	31.64	18.671(0.037)	31.63	18.504(0.044)	31.64	18.210(0.041)	31.64	18.180(0.039)
32.63	19.920(0.064)	32.62	19.016(0.034)	32.63	18.729(0.039)	32.62	18.524(0.033)	32.63	18.351(0.033)	32.64	18.219(0.040)
36.60	20.201(0.125)	36.59	19.294(0.060)	36.60	18.918(0.040)	36.59	18.796(0.046)	36.60	18.548(0.037)	36.60	18.394(0.043)
37.63	20.232(0.101)	37.64	19.347(0.059)	$\cdots$	$\cdots$	37.63	18.734(0.042)	37.62	18.515(0.038)	37.62	18.468(0.056)
38.65	20.038(0.115)	38.63	19.399(0.069)	38.64	18.969(0.042)	38.63	18.726(0.037)	38.64	18.487(0.033)	38.64	18.385(0.040)
39.65	20.276(0.109)	39.63	19.332(0.048)	39.64	19.015(0.043)	39.64	18.688(0.047)	39.64	18.456(0.034)	39.64	18.380(0.044)
40.62	20.427(0.107)	40.60	19.459(0.036)	40.61	18.967(0.029)	40.61	18.803(0.042)	40.61	18.484(0.035)	40.61	18.381(0.048)
41.61	20.562(0.166)	41.62	19.439(0.039)	41.60	19.096(0.042)	41.62	18.810(0.042)	41.60	18.607(0.036)	41.60	18.376(0.038)

Notes. [a]JD+2456900.

Table 4. NIR photometry of AT 2014ej in the du Pont (+RetroCam) "natural" system.

JD	Photometry	Error	Filter
2456929.64	17.51	0.02	Y
2456931.58	17.58	0.03	Y
2456932.58	17.68	0.03	Y
2456929.67	17.24	0.02	J_{rc2}
2456931.62	17.35	0.03	J_{rc2}
2456932.61	17.47	0.03	J_{rc2}
2456929.66	16.79	0.03	H
2456931.61	16.92	0.03	H
2456932.60	17.05	0.03	H
2456937.59	16.17	0.14	K_s [a]

Notes. The uncertainties in photometry correspond to the sum in quadrature of the instrumental photometric error and the nightly zero-point error. [a]Observations were obtained with the *Baade* (+FourStar) telescope, and the photometric zero-point was computed relative to two 2MASS stars. Also note that no template subtraction was performed on this single science image.

Table 5. CHASE unfiltered filter photometry of AT 2014ej.

MJD	O [a]	Telescope
56910.27	>18.3	PROMPT4
56920.06	17.519(054)	PROMPT1
56930.32	18.286(121)	PROMPT4
56940.05	18.668(165)	PROMPT1
56941.27	18.656(318)	PROMPT3
56943.04	18.699(158)	PROMPT4
56943.27	18.527(090)	PROMPT1
56956.24	18.217(118)	PROMPT4
56958.10	18.043(072)	PROMPT1
56959.23	18.106(088)	PROMPT4
56961.05	18.119(085)	PROMPT4
56978.13	17.669(102)	PROMPT4
56983.07	17.886(079)	PROMPT4
56998.12	18.025(148)	PROMPT4
57015.08	18.361(124)	PROMPT3

Notes. [a]Unfiltered photometry calibrated relative to the CSP-II *r*-band local sequence.

Table 6. NIR photometry of AT 2014ej from PESSTO.

MJD	Photometry	Error	Filter
56944.163	17.07	0.08	J
56944.163	16.97	0.09	H
56944.163	16.37	0.08	K
56954.000	16.39	0.05	K
56964.250	16.09	0.08	K

Notes. Observations were obtained with the NTT(+SOFI) telescope, and the photometric zero-point was computed relative to 2MASS stars.

As NGC 7552 is a member of the Grus Quartet, we turn to distance estimates of the group itself as well as to the individual members NGC 7582, NGC 7590, and NGC 7599. NED lists five different Tully–Fisher distances for NGC 7582, with the most recent being $\mu = 31.76 \pm 0.20$ mag. NED also lists a handful of Tully–Fisher distances to NGC 5790, with the most recent being from the Cosmicflows-2 catalog (Tully et al. 2013), corresponding to $\mu = 32.46 \pm 0.20$ mag. Finally, NED also lists a variety of Tully–Fisher distances for NGC 7599, with the two most recent values coming in as $\mu = 31.22 \pm 0.20$ mag from the Cosmicflows-2 catalog (Tully et al. 2013) and $\mu = 31.02 \pm 0.45$ mag from the Cosmicflows-3 catalog (Tully et al. 2016).

NGC 7582 and NGC 7552 are interacting, as is shown by tidal extension of HI between the galaxies (Dahlem 2005). The distance modulus of NGC 7582 is $\mu = 31.76 \pm 0.20$ mag, in agreement with the distance modulus of NGC 7552 as computed from its redshift. In the following, we adopt $\mu = 31.72 \pm 0.15$ mag as the distance modulus to NGC 7552.

Finally, in Appendix A we compute the host metallicity using a spectrum of NGC 5775 obtained by the Sloan Digital Sky Survey (SDSS), while Appendix B contains details on the total reddening value used in this work. In short, we find the metallicity at the location of AT 2014ej to be super-solar, and our best estimate for the total visual extinction of AT 2014ej is $A_V^{\rm tot} = 0.96 \pm 0.47$ mag.

2.2. Observations

The CSP-II obtained 20 epochs of optical *ugriBV*-band imaging with the Swope (+CCD camera) telescope, extending between

Table 7. Journal of spectroscopic observations of AT 2014ej.

Object	Date (JD)	Date (UT)	Days since discovery [a]	Telescope	Instrument	Resolution (Å)
AT 2014ej	2456927.67	September 27.16	+7.1	du Pont	WFCCD	7.5
AT 2014ej	2456930.60	September 30.10	+10.0	NTT	EFOSC2	15.8/16.0 [b]
AT 2014ej	2456931.59	October 01.09	+10.6	*Clay*	MIKE	0.21
AT 2014ej	2456933.96	October 03.46	+13.3	ANU	WiFeS	0.98
AT 2014ej	2456953.62	October 23.12	+32.9	NTT	EFOSC2	15.8/16.0
AT 2014ej	2456963.61	November 02.11	+42.8	NTT	EFOSC2	15.8/16.0
AT 2014ej	2456992.57	December 01.07	+71.6	NTT	EFOSC2	15.8/16.0

Notes. [a]Days since outburst assuming outburst date for AT 2014ej of 24.06 September 2014 UT (JD−2456924.56). [b]NTT (+EFOSC) observations were obtained with two grisms, i.e., Gr#11 and Gr#16, providing slightly different spectral resolutions.

Table 8. PESSTO *V*-band photometry from acquisition images of AT 2014ej.

MJD	V [a]	Telescope
56930.095	18.458(0.031)	NTT
56953.095	18.566(0.036)	NTT
56963.080	18.389(0.037)	NTT
56992.070	18.195(0.045)	NTT

Notes. [a]*V*-band photometry calibrated relative to the CSP-II *V*-band local sequence listed in Table 1.

Table 9. Spectrophotometry of AT 2014ej in the Swope "natural" system.

JD	B	g	r	i
2456927.67	18.709	18.446	17.967	17.898
2456930.60	18.821	18.574	18.156	. . .
2456933.96	. . .	. . .	18.449	18.425
2456953.62	19.199	18.904	18.324	18.209
2456963.61	18.992	18.693	18.166	18.005
2456992.57	18.776	18.496	17.959	17.802

Notes. We assume a conservative error of 0.1 mag on the spectrophotometry due to the fact that there might be host galaxy flux contaminating the spectra.

Table 10. Adopted color excess values and distance moduli for the LRN sample compared to AT 2014ej.

LRN	μ (mag)	$E(B-V)_{\rm tot}$ (mag)
SN 1997bs	29.82	0.21
NGC 3437-2011-OT1	31.60	0.02
NGC 4490-2011-OT1	29.91	0.32
UGC 12307-2013-OT1	32.99	0.22
M101-2015-OT1	29.04	0.008
SNhunt248	31.76	0.045
AT 2017jfs	32.73	0.022
AT 2018hso	31.64	0.30

+5 d to +37 d relative to first detection[2]. In addition, three epochs of NIR *YJH*-band imaging were obtained with the du Pont (+RetroCam) telescope between +9 d to +12 d, as well as a single epoch of K_s-band photometry taken with the *Magellan Baade* telescope equipped with the FourStar imager (Persson et al. 2013) on +17 d.

CSP-II photometry of the transient was computed relative to an optical/NIR local sequence consisting of 27/7 stars, themselves calibrated relative to standard star fields observed over multiple photometric nights. Optical (*ugriBV*) and NIR (*YJH*) photometry of the local sequence stars in the "standard" system are listed in Tables 1 and 2, respectively. Optical photometry of AT 2014ej in the "natural" photometric system is listed in Table 3, while Table 4 lists the NIR photometry also in the CSP-II natural system. Finally, a single K_s-band epoch of photometry was calibrated relative to 2MASS stars in the field of NGC 7552 and is also listed in Table 4.

AT 2014ej was observed by CHASE (Pignata et al. 2009) with the PROMPT telescopes (Reichart et al. 2005) located at CTIO. We detect AT 2014ej in 14 epochs of unfiltered images. This includes the earliest detection and the subsequent detection in survey search images extending over +95 d. The images were reduced following standard procedures, and photometry of AT 2014ej was computed relative to the *r*-band photometry of the CSP-II local sequence of stars in the field of the host galaxy. Prior to computing photometry, a deep host-galaxy template image was constructed and used to subtract the host light at the position of the transient. The stacked images were obtained prior to the discovery of AT 2014ej. Unfiltered photometry obtained with the PROMPT telescopes is listed in Table 5.

PESSTO obtained a handful of *JHK*-band images with the NIR imager SOFI (Son OF ISAAC; Moorwood et al. 1998)

attached to the ESO New Technology Telescope (NTT)[3]. Point-spread function (PSF) photometry of the transient was calibrated relative to 2MASS stars in the field of NGC 7552, and the results are listed in Table 6. This includes a single epoch of *JH*-band photometry and three epochs of *K*-band photometry.

Five epochs of low-resolution visual wavelength spectroscopy of AT 2014ej were obtained between +7 d to +72 d, and these observations are summarized in Table 7. These spectra include data taken by the CSP-II with the du Pont (+WFCCD) telescope and by PESSTO with the NTT (+EFOSC2) and a previously published spectrum obtained with the ANU telescope (+WiFes; Childress et al. 2016). The spectroscopic data

---

[2] First detection of AT 2014j was made by CHASE and occurred on JD-2456920.56.

[3] See details in the PESSTO third data release documentation located at the url `http://www.eso.org/rm/api/v1/public/releaseDescriptions/88`
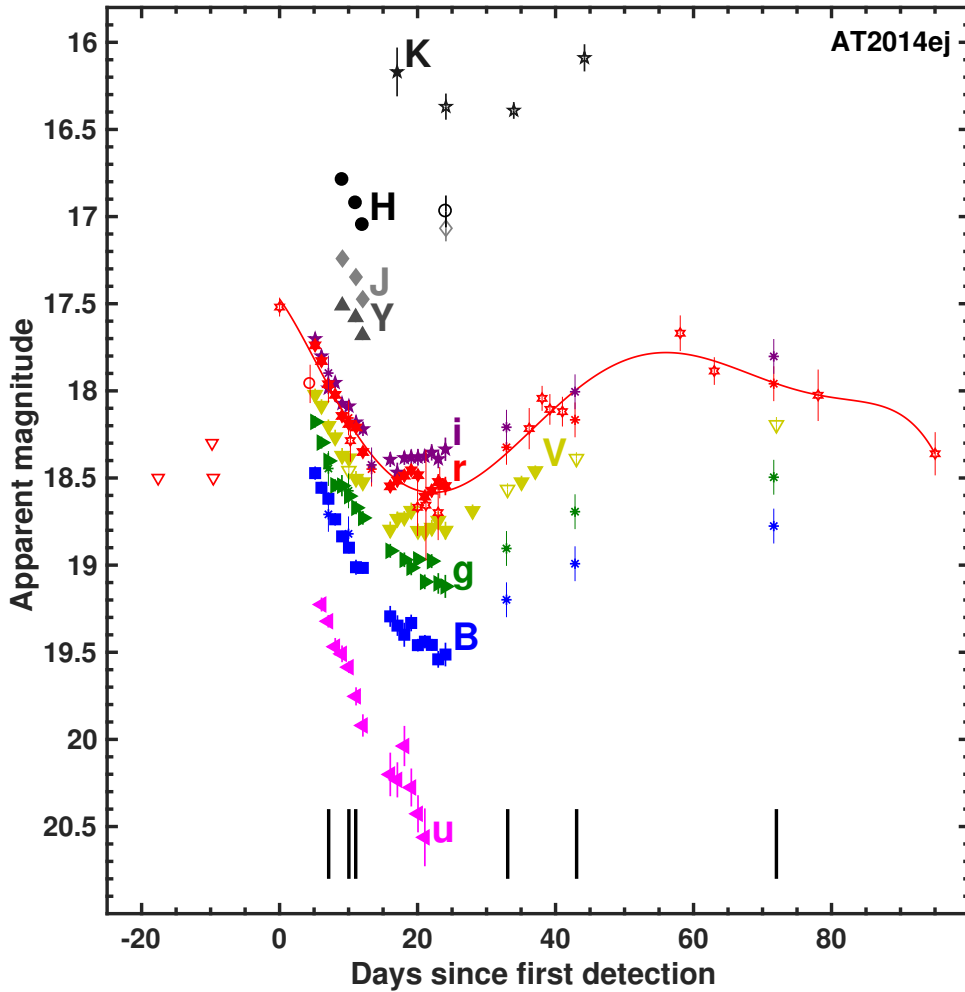
Fig. 2. Optical and NIR light curves of AT 2014ej. The light curves decline rapidly over the first ~20 days when they appear to reach a minimum and then evolve to a second peak (around 60 days in *r* band). The open red circle is the BOSS discovery magnitude, while open red triangles at 18.5 mag correspond to nondetection limits reported by Bock et al. (2014), and the open red triangle at 18.3 is a nondetection limit determined from an unfiltered CHASE image. Open red stars are CHASE photometry, and open yellow triangles and open symbols in the NIR bands are PESSTO (EFOSC2 and SOFI) photometry (*V*, *J*, *H*, *K*). Colored asterisks are spectrophotometry (*B*, *g*, *r*, *i*). The other colored filled markers are CSP-II photometry. The optical *r*-band light curve is fit with a low-order polynomial shown as a solid red line. Optical spectral phases are marked by black segments.

were reduced following standard procedures. In addition to these low-resolution spectra, a single medium-dispersion spectrum was obtained on +11 d with the 6.5 m *Magellan Clay* telescope equipped with MIKE (*Magellan* Inamori Kyocera Echelle; Bernstein et al. 2003). The MIKE spectrum followed standard procedures and made use of IRAF[4] echelle routines and the `mtools` standard package developed by Jack Baldwin.

Finally, we note that the *V*-band acquisition images taken in the process of obtaining spectroscopic followup of AT 2014ej with the NTT were used to measure *V*-band photometry in four different epochs, three of which occurred after the end of the CSP-II NIR followup. PSF photometry of AT 2014ej was computed from these images and calibrated relative to the CSP-II *V*-band local sequence. The resulting photometry is listed in Table 8. With the *V* band from CSP-II and PESSTO acquisition images, we performed an absolute flux calibration of the spectra, and from these, we obtained spectrophotometry in the *Bgri* bands. Because the host galaxy flux might be contaminated, we assumed a conservative 0.1 mag error on spectrophotometry, which is listed in Table 9. Spectrophotometry was useful to cover *Bgi* bands at epochs after +24 d.

3. Results

3.1. Photometry, broadband colors, and SEDs

Photometry of AT 2014ej is plotted in Fig. 2. Post detection, the optical light curves decline in brightness, exhibiting a drop between 0.5 to 1.0 mag over the first ten days. This decline continues in all bands out to ≥+15 d. Subsequently, as the *u* band continues to exhibit a rapid drop in brightness, the *B*- and *g*-band light curves significantly slow down in their rate of decline, while the *V*-, *r*-, and *i*-band light curves exhibit a plateau phase that last about ten days. In the CHASE *r*-band data, the PESSTO *V*-band images, and spectrophotometry in *Bgri* bands, we observe a rise in the light curves from each of these optical bands after +24 d. The rise in the *r* band goes from 18.5 mag up to 17.7 mag between +24 d and +60 d, followed by a shallow decline reaching 18.4 mag at +95 d.

The first CHASE detection of AT 2014ej reveals a peak apparent magnitude of ≤17.5, corresponding to a peak absolute magnitude of $M_r \leq -15.09 \pm 0.48$, given the assumed extinction and distance modulus. The accompanying uncertainty is computed by adding in quadrature the errors in adopted reddening and distance. Taking an average between the dates of last nondetection and first detection, we estimate an outburst date of JD = 2456915.75 ± 4.80.

In the three top panels of Fig. 3 we plot the intrinsic optical colors of AT 2014ej compared to those of known LRNe candidates: SN 1997bs (Van Dyk et al. 2000; Pastorello et al. 2019a), NGC 3437-2011-OT1 (Pastorello et al. 2019a),
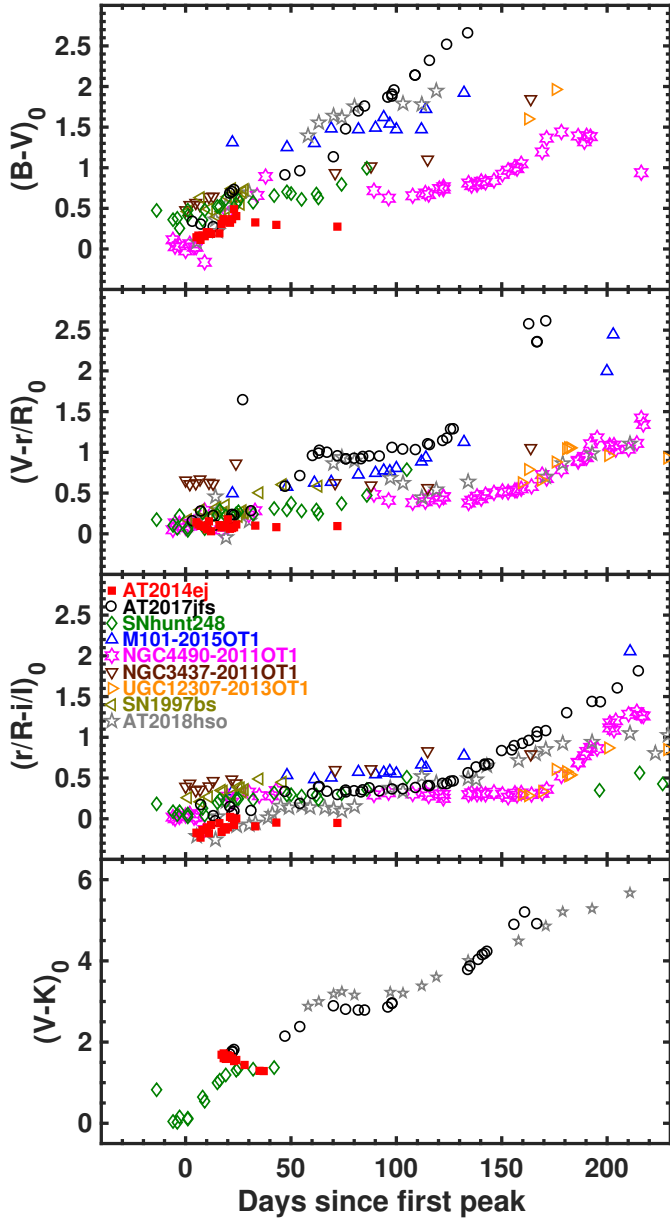
---

[4] IRAF is distributed by the National Optical Astronomy Observatory, which is operated by the Association of Universities for Research in Astronomy (AURA) under cooperative agreement with the National Science Foundation.

Fig. 3. Intrinsic broadband color evolution of AT 2014ej compared to other well-observed LRNe, including SN 1997bs (Van Dyk et al. 2000), NGC 3437-2011-OT1 (Pastorello et al. 2019a), NGC 4490-2011-OT1 (Pastorello et al. 2019a), UGC 12307-2013-OT1 (Pastorello et al. 2019a), M101-2015-OT1 (Blagorodnova et al. 2017), SNhunt248 (Kankare et al. 2015), AT 2017jfs (Pastorello et al. 2019b), and AT 2018hso (Cai et al. 2019). The colors plotted were corrected for both Milky Way and host-galaxy reddening using the values summarized in Table 10.

NGC 4490-2011-OT1 (Pastorello et al. 2019a), UGC 12307-2013-OT1 (Pastorello et al. 2019a), M101-2015-OT1 (Blagorodnova et al. 2017), SNhunt248 (Kankare et al. 2015), AT 2017jfs (Pastorello et al. 2019b), and AT 2018hso (Cai et al. 2019). The comparison objects have been corrected for reddening, adopting $E(B-V)_{tot}$ color excess values listed in Table 10.

Our observations of AT 2014ej cover the first +71 d of color evolution corresponding to the object's first and second peak. At the earliest epochs, the intrinsic $(B-V)_0$ color is ≈0. This places it among the bluest objects in the comparison sample, similar to NGC 4490-2011-OT1. Over the period following the

first light-curve peak, up to +24 d, the colors of AT 2014ej also evolve very similarly to those of the comparison sample. Close inspection reveals that the $(B-V)_0$ colors of AT 2014ej evolve rapidly to red, similar to the comparison sample. However, during the rise and after the second peak, the $(B-V)_0$ and $(V-r)_0$ colors of AT 2014ej are clearly bluer than those of the other objects.

To conclude our investigation into the color curves of AT 2014ej, we plot in the bottom panel of Fig. 3 is its intrinsic $(V-K)_0$ color curve along with those of AT 2017jfs, SNhunt128, and AT 2018hso. Although the temporal coverage of AT 2014ej is relatively limited, its colors match those of the comparison objects well during the overlapping phases. This provides additional confidence that AT 2014ej is indeed an LRN.

We constructed the spectral energy distributions (SEDs) of AT 2014ej following the same procedure as for SNhunt120 (see Paper I, Sect. 3.1). We plot in Fig. 4 the reddening-corrected SEDs of AT 2014ej. These SEDs are relatively well reproduced by a single blackbody (BB) at all epochs (red solid line in the left panel), including the epochs when some NIR ($YJHK_s$) photometry is also available. Because of line blanketing, the u-band flux points lie below the fitted BB function. To facilitate a more consistent comparison of the bolometric properties at epochs with different wavelength coverage, we also present a single BB fit limited to the bands in common at all epochs, that is, from B to i, and this is plotted as dashed blue lines in the left panel. Because the u band was excluded, we obtain BB curves that tend to peak at bluer wavelengths than when we include all the bands in our BB fitting.

On +9 d, +11 d, +12 d, +17 d, +23.9 d, and +32.9 d, we have NIR broad-band measurements. When plotted along with the other flux points in log-log space, they reveal a non-negligible excess of flux in the K_s band, as compared to the single BB fit (including and excluding u band), which might be an indication of dust emission at redder wavelengths. These six SEDs are plotted in Fig. 5 along with single BB fits that include and exclude the u-band flux point. A conclusively determination whether the K_s excess is due to dust emission would require mid-IR (MIR) observations, which unfortunately were not taken.

The BB-radius and BB-temperature profiles associated with the photosphere and the bolometric light curve of AT 2014ej are also plotted in Fig. 4. Profiles for both of these parameters are shown for fits including all the bands and fits only including between the B and i bands. Excluding the u band produces a radius that is smaller by about 0.05×10^{15} cm than including it, and a higher temperature by about ∼1000 K. The BB luminosity does not change significantly between the two BB fit approaches. The bolometric properties obtained by fitting a BB over the wavelength range including the B and i bands show that the BB radius initially declines from ∼0.25×10^{15} cm to below 0.2×10^{15} cm, and then, beginning at about +20 d, rises to 0.6×10^{15} cm. The BB temperature declines from ∼10 000 K to ∼7000 K, followed by an increase to 8000 K during the rise to and following the second peak.

After the initial (until +15 d) decline (from 3.0 to 1.3 × 10^{41} erg s^{-1}), the luminosity remains almost constant, reaching ∼1.2×10^{41} erg s^{-1} at +24 days. The complete multiband CSP-II light-curve data of AT 2014ej only extend to +24 d. However, when we consider the CHASE r-band light curve, the PESSTO V- and K_s-band data, and spectrophotometry, we can add a few points that show a rebrightening at +33 d, +43 d and +72 d, forming a second peak. When we convert the CHASE absolute r band to a bolometric luminosity assuming $M_r \approx M_{Bol}$, the luminosity evolution of AT 2014ej is extended up to +95 d. This is
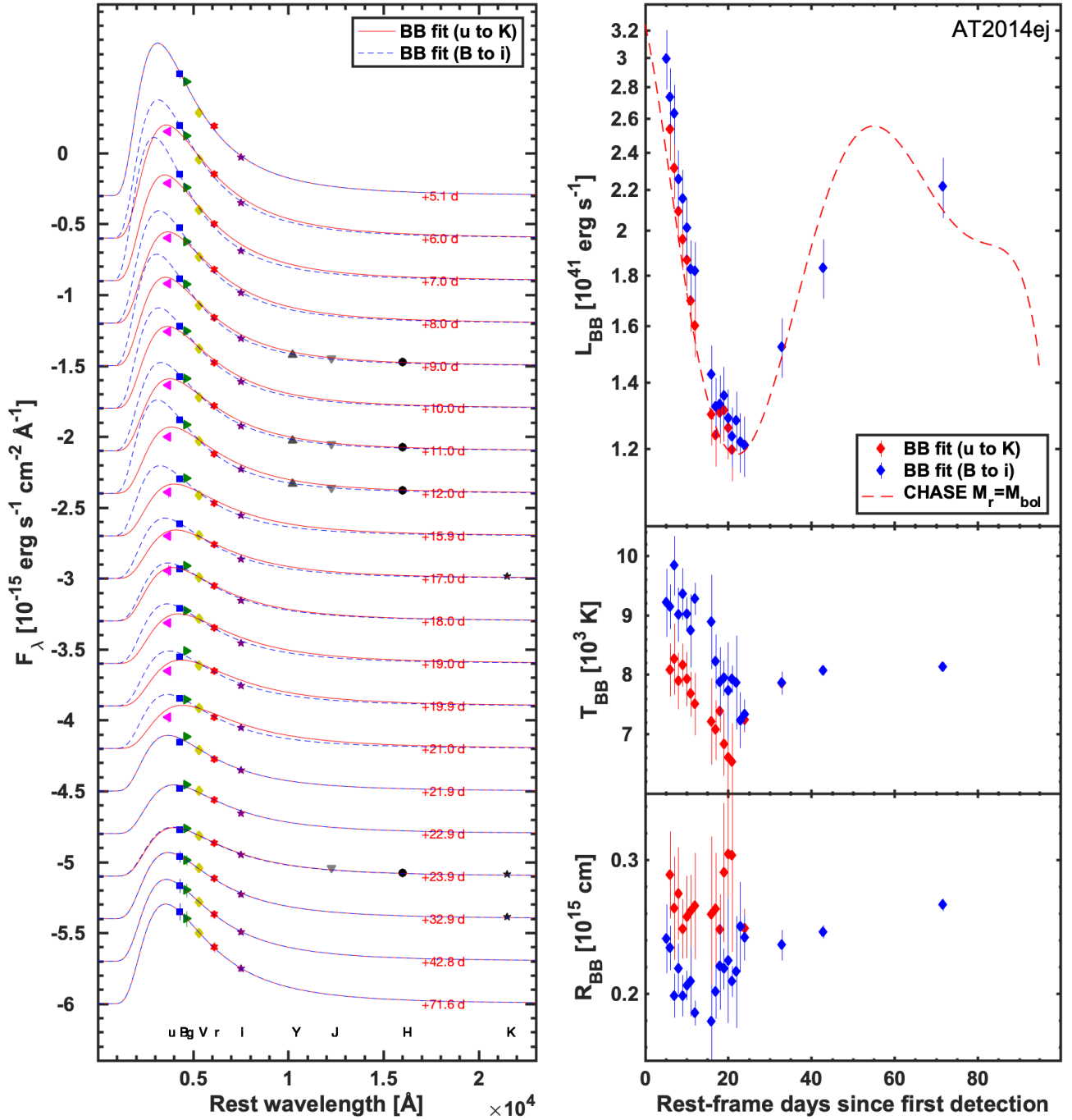
Fig. 4. *Left*: SEDs of AT 2014ej constructed from photometry obtained between +5.1 d and +71.6 d post discovery. On each SED we overplot its best-fit BB function (solid red line) including all the available data from u to K_s, and its best-fit BB function (dashed blue line) including only the filters in common for all the epochs, namely B to i. *Right*: estimates of BB luminosities (from the BB fit integrations and from the CHASE r band) (*top*), BB temperatures (*middle*), and BB radii (*bottom*).

overplotted in the top right panel of Fig. 4 as the dashed line. The r band reproduces the bolometric light curve rather well after the initial epochs when the flux comes predominantly from bluer wavelengths. If our assumption is valid, the luminosity has a second peak that reaches a luminosity of 2.6×10^{41} erg s^{-1}.

3.2. Spectroscopy

Six epochs of low-resolution visual wavelength spectra of AT 2014ej are plotted in Fig. 6; they extend between +7 d

and +72 d relative to first detection. The main features characterizing the spectra are the narrow Balmer lines in emission and Ca II H&K in absorption. The spectral continuum becomes redder with time. The velocities of the lines, corrected for the spectral resolution, are shown in the top panel of Fig. 7, where the Balmer lines are shown to have a full width at half-maximum (FWHM) of about 900 km s^{-1}, while the Ca II absorption exhibits lower velocities and is unresolved. In the ANU (+WiFeS) spectrum at +13.3 d, which has a higher resolution than the NTT (+EFOSC2) spectra, it is possible to see that the
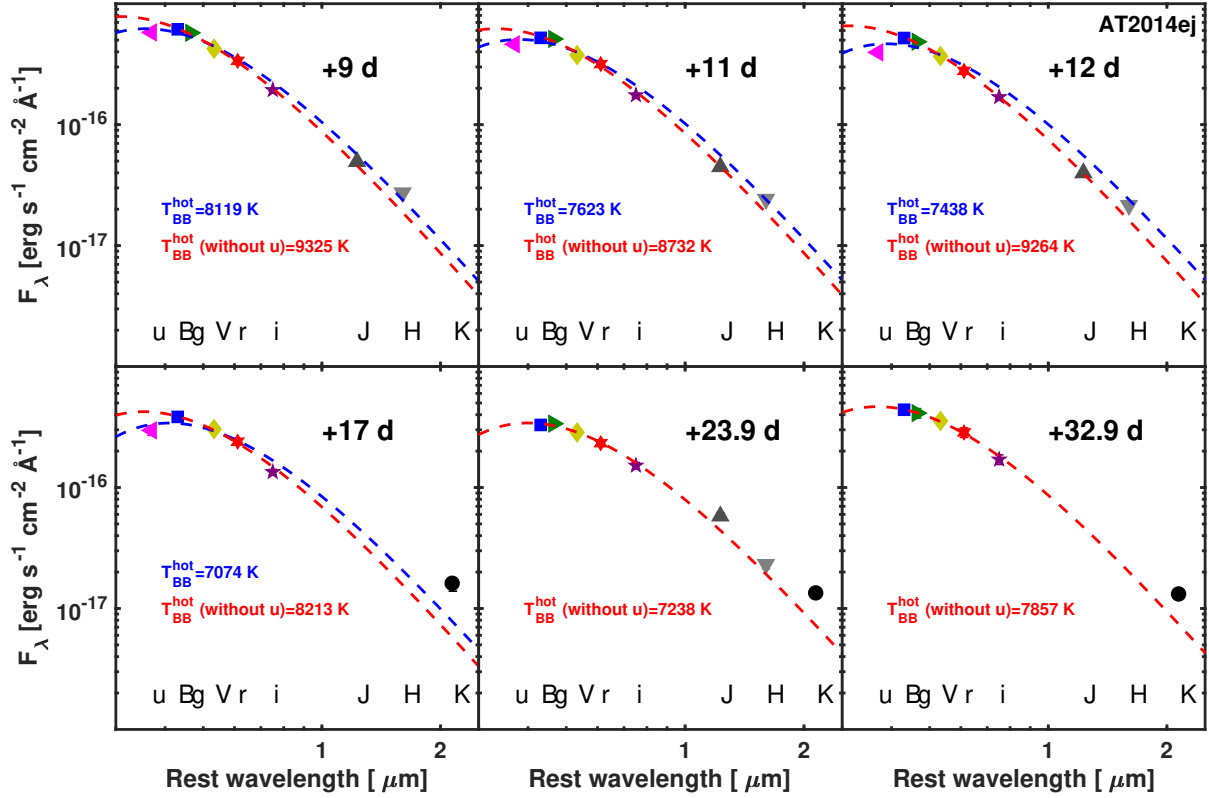
Fig. 5. SEDs of AT 2014ej, constructed with *uBgVri*- and *JHK$_s$*-band flux points for the six epochs where at least some NIR observations are available. The phase of each SED is reported in black in each panel. The flux points are fit with a single BB function including (dashed blue line) and excluding (dashed red line) the *u*-band flux measurement. The three epochs of *K$_s$*-band flux points suggest an excess of flux relative to the best-fit single BB function, and this applies regardless of whether the *u*-band flux point is included in the fit. This *K$_s$*-band excess could be indicative of dust emission, but without MIR coverage, it is difficult to be conclusive.
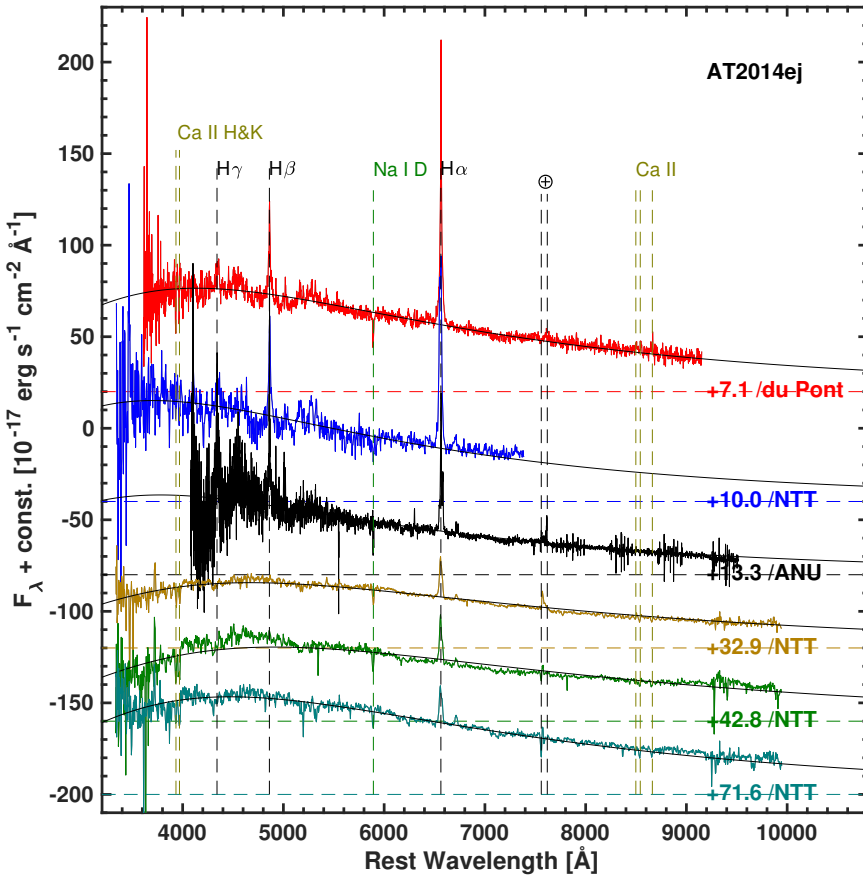
Fig. 6. Low-resolution reddening-corrected visual wavelength spectra of AT 2014ej plotted in the rest-frame. The spectra are offset from one another in flux space by the addition of an arbitrary constant for presentation purposes. Epochs of observations relative to the discovery date are provided, along with the labeling of key spectral features, and the positions of two prevalent telluric features are indicated with an Earth symbol. The solid black lines correspond to BB fits. The BB fits exclude the wavelength ranges that contain strong emission lines.
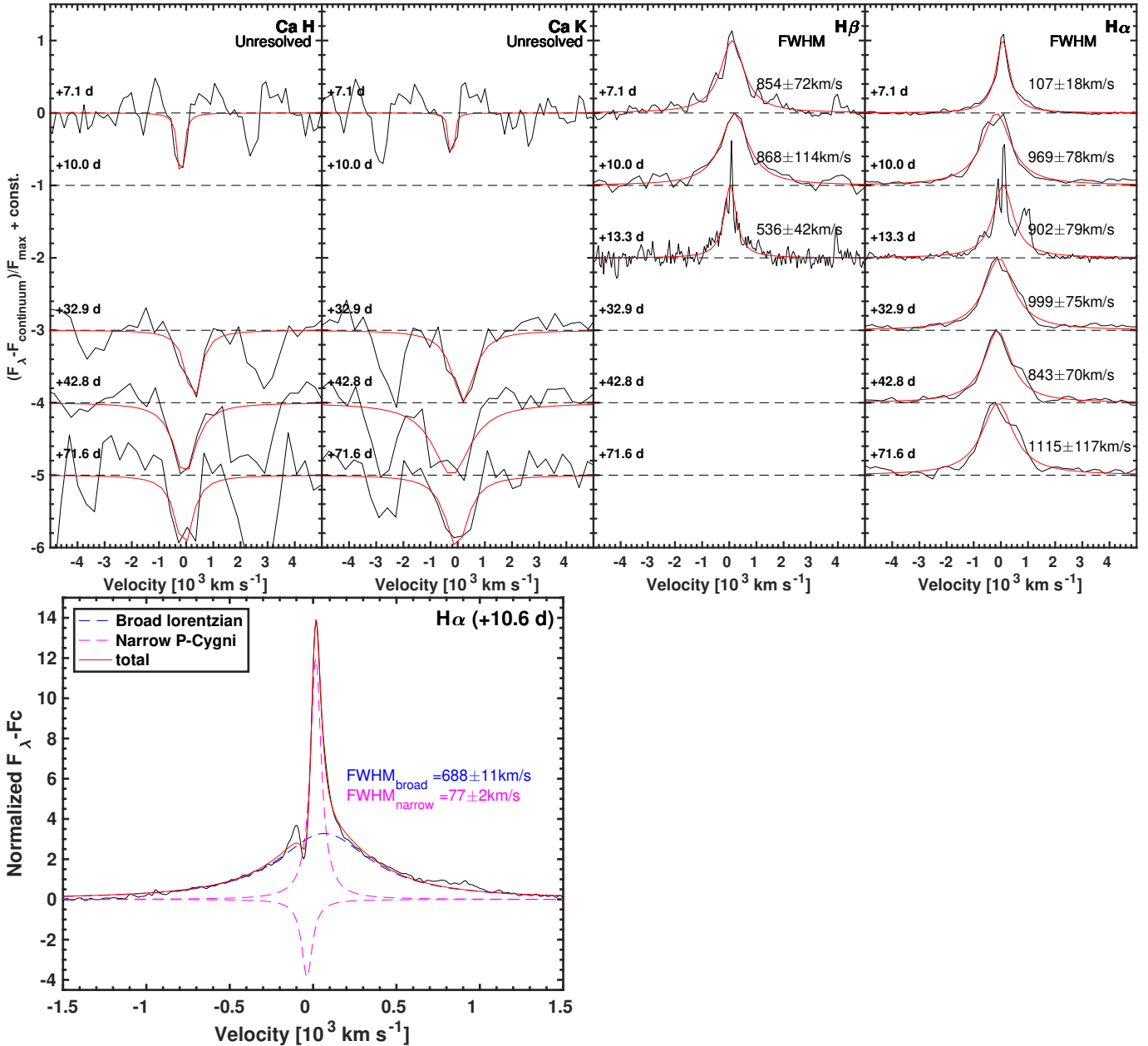
Fig. 7. *Top*: spectral features of AT 2014ej including the Ca II H&K, Hβ, and Hα lines. The continuum of each spectrum was fit using a low-order polynomial and was subtracted from the data. The Lorentzian line profile fits are overplotted with a red line, and the corresponding line velocities are listed and also provided in Table 11. *Bottom*: MIKE spectrum around Hα in velocity space. The profile is well fit by two components consisting of a broad Lorentzian and a narrow P Cygni profile (sum of two Lorentzians with the same width) whose FWHMs are reported in the figure.

presence of [N II] from the host galaxy modifies the Hα profile. The spectrum also indicates a narrow P Cygni profile for Hα and Hβ.

The higher dispersion MIKE spectrum obtained on +11 d is shown in Fig. 8 and reveals a clear narrow P Cygni component associated with each of the spectral features that are plotted (in velocity space) in Fig. 9. The narrow Hα P Cygni feature is measured to have a blue velocity at zero intensity (BVZI) of 106 ± 6 km s^{-1} and a P Cygni minimum velocity of 66 ± 6 km s^{-1}. This line component is observed in many SNe IIn and is thought to be formed from outer unshocked circumstellar material (CSM) that is excited by the emission originating from the shock region (see, e.g., Kiewe et al. 2012; Taddia et al. 2013; Nyholm et al. 2020). As a result, the BVZI value of this component provides a measure of the CSM velocity.

In the bottom panel of Fig. 7 we show the entire profile of the Hα line in the MIKE spectrum. This is well reproduced by two components, a narrow P Cygni (given by two Lorentzians, one in emission and one in absorption) and a broader Lorenzian emission. The broad component has a velocity of about 690 km s^{-1}, whereas the narrow one has an FWHM of about 80 km s^{-1}. These two components are not visible in the spectra with lower resolution (with the possible exception of the ANU spectrum) that are shown in the top panel of Fig. 7. The broader Lorentzian component in the H lines shown here could form from electron scattering, which would alter the narrow emission profile to a broader profile in a region in close proximity to the location of the CSM interaction.

The BVZI and absorption minimum velocities are approximately 100 km s^{-1} for all the lines except for Ca II H&K, where
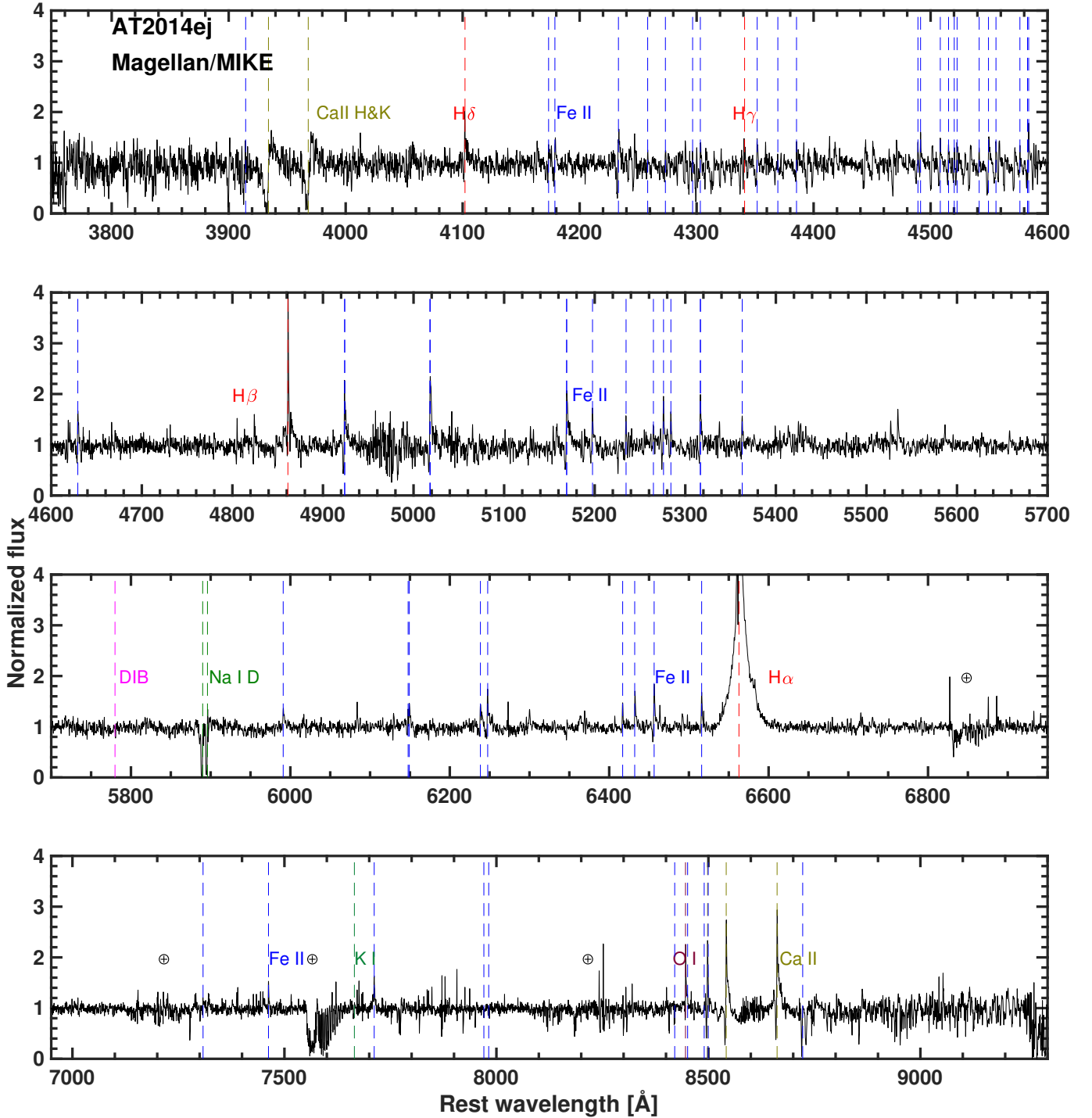
Fig. 8. Medium-resolution visual-wavelength spectrum of AT 2014ej obtained with the *Magellan Clay* (+MIKE) telescope on +11 d and plotted in the rest-frame. Key spectral features are labeled, and prominent telluric features are marked with an Earth symbol.

the BVZI is about 500 km s^{-1}. The higher velocity inferred from the Ca II H&K feature might arise because it originates from material that is ejected during a massive binary merger.

3.3. Progenitor constraints

NGC 7552 was observed on a number of occasions with the HST (+WFPC2) prior to the discovery of AT 2014ej. Unfortunately, the location of AT 2014ej lies a few pixels outside the field of view of WFPC2 in the earliest images taken in 2015

April. However, 2×600 s *F*218*W* images were obtained with HST (+WFC3) on 1999 March 31 that do cover the position of AT 2014ej. Here only the center of the galaxy was clearly visible in the *F*218*W* data, and the lack of reference sources in the field prevents us from obtaining any precise astrometry. We therefore performed photometry with HSTPHOT on a region contained within a 40×40 pixel box centered on the coordinates of the transient, and extracted all sources detected with a >5-sigma significance. Within this region lies no source. With no candidate source in the region of the transient, we set an upper
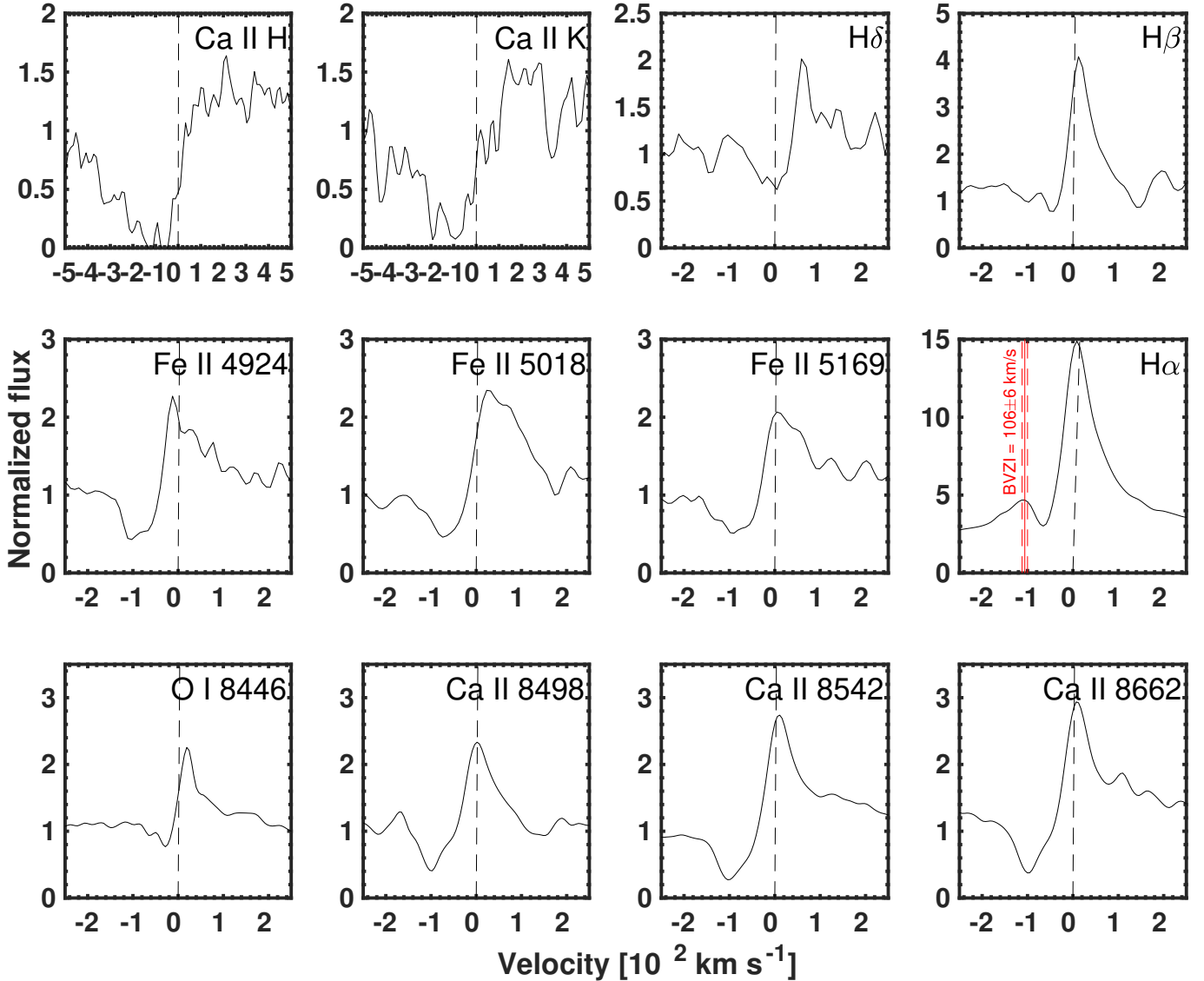
Fig. 9. AT 2014ej line profiles of prominent emission lines in the medium-resolution MIKE spectrum (see Fig. 8), plotted in velocity space. This includes Ca II H&K, Balmer lines of Hδ, Hβ, and Hα, the Fe II multiplet 42, O I λ8446, and the Ca II NIR triplet. The vertical dotted lines mark the rest-velocity positions of the ions. The red line in the Hα panel marks the BVZI of $106 \pm 6 \, \mathrm{km \, s^{-1}}$.

$F218W > 20.3$ mag limit determined from the average magnitude of all point sources in the field with a 5-sigma detection.

A further set of pre-outburst images covering the site of AT 2014ej was taken between 2009 May 5−6 with HST (+WFPC2). This includes deep images with the broadband filters $F336W$ (4400 s), $F439W$ (1800 s), $F555W$ (520 s), and $F814W$ (520 s), and as well with a narrow-band Hα (1800 s) filter. The field of view (FOV) afforded by HST (+WFPC2) is smaller than that of our post-outburst ground-based CSP-II data, and it is challenging to align the two images to precisely localize the position of AT 2014ej in the HST images. Using five sources common to both images, we find that the position of AT 2014ej lies at x, y pixel coordinate (75, 172) on the $F555W$ image.

While the formal uncertainty in the geometric transformation between pre- and post-outburst images is <1 WFPC2 pixel (=0″.1), this probably is an underestimate due to the small number of sources used for the alignment. Adopting a conservative approach, we computed photometry for all sources detected at a >5-sigma significance within 1″ of the position of AT 2014ej, which might possibly be progenitor candidates. None of the

sources are measured to be brighter than the apparent magnitude $m_{F814W} \sim 23$. These sources are indicated in Fig. 10, along with the location of AT 2014ej. Here the area enclosed within the circle accounts for the uncertainty in the estimated position of AT 2014ej.

4. Discussion

4.1. AT 2014ej compared with luminous red nova candidates

Here the similarities between the observational properties of AT 2014ej to those of other LRNe are assessed. First we present a spectral comparison between AT 2014ej and the well-observed LRN AT 2017jfs, and then we compare the light curves of AT 2014ej to AT 2017jfs and an expanded sample of LRNe from the literature.

Visual wavelength spectra of AT 2014ej and AT 2017jfs are plotted in Fig. 11. At early times, which coincide with their first peak (see below), the two objects are strikingly similar, exhibiting nearly identical narrow spectral features, most notably,
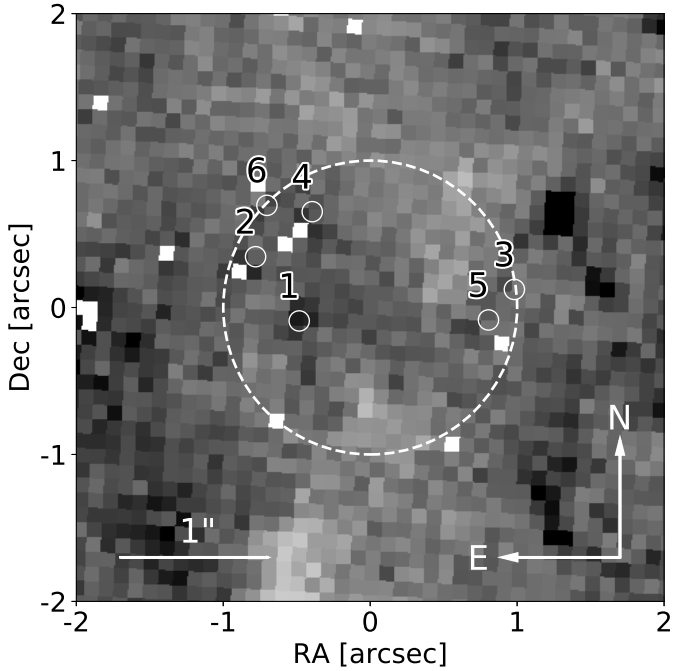
Fig. 10. Archival HST (+WFPC2) *F555W*-band image of NGC 7552. The position of AT 2014ej is indicated with a circle, and the positions of sources detected within 1″ are numbered. Because most sources detected in this region have a low S/N, they are not particularly obvious on visual inspection. White squares are aberrant pixels that have been masked.

narrow Balmer emission lines and some metal lines blueward of Hβ. As the two objects evolve toward their second peak (see below), the strength of Hα decreases while the Hβ feature disappears. Furthermore, beyond +60 d, the Hα continues to decrease in AT 2014ej and becomes absent in AT 2017jfs. During the same period, the spectra of AT 2017jfs evolve further to the red, while those of AT 2014ej on +71.6 d show little evolution. This behavior may be linked to AT 2014ej being brighter than AT 2017jfs at these phases (see below). Unfortunately, we lack spectral observations of AT 2014ej at even later phases, and are therefore unable to document the expected emergence of molecular overtones consistent with the spectrum of a late-type star and the restrengthening of Hα, as seen in LRNe such as AT 2017jfs (Pastorello et al. 2019b).

In Fig. 12 the absolute magnitude light curves of AT 2014ej are compared to those of eight other LRN candidates, including: SN 1997bs, NGC 3437-2011-OT1, NGC 4490-2011-OT1, UGC 12307-2013-OT1, M101-2015-OT1, SNhunt248, AT 2017jfs, and AT 2018hso. The comparison light curves have been adjusted for reddening and placed on the absolute magnitude scale, for which we adopted the color excess values and the distance moduli listed in Table 10. Although the light curve of AT 2014ej is limited in phase coverage, its shape and absolute magnitudes resemble the double peak of the other well-observed LRNe. In particular, the *V* and *r* bands evolve very much like that of AT 2017jfs. The CHASE unfiltered light curve of AT 2014ej reveals a second peak that is ≲0.23 mag fainter than at discovery. The strength and phase of the secondary peak of AT 2014ej is similar to that of SNhunt248; it occurs about 100 d earlier than the peaks of M101-2015-OT1 and NGC 4490-2011-OT1, both of which exhibit a second peak that occurs well after +100 d.

We conclude this part of the analysis with a return to Fig. 1 of Paper I, which compares the peak absolute *r*-band magnitude

Table 11. FWHM velocity measurements of prominent spectral features in AT 2014ej.

Phase [a] (d)	Hβ (km s^{-1})	Hα (km s^{-1})
+7	854 ± 72	107 ± 18
+10	868 ± 114	969 ± 78
+33	⋯	999 ± 75
+43	⋯	843 ± 70
+72	⋯	1115 ± 117

Notes. [a]Phase with respect to date of discovery.

with the *r*-band light curve decay (defined as the time in days for the light curve to drop one magnitude). Our lower limit value of AT 2014ej places it well within the parameter space that is populated by other well-observed LRNe. When we consider that AT 2014ej was discovered somewhat past its first peak, it is clearly one of the brightest LRN studied so far (see below).

4.2. Direct observational evidence for linking (luminous) red novae to common-envelope events

Because a common-envelope (CE) phase is short (about 10^3 yr, Meyer & Meyer-Hofmeister 1979; Podsiadlowski 2001), it is extremely rare to detect this ephemeral phase of stellar evolution. Nevertheless, a number of candidates for direct observations of CE events have been proposed, with a prime candidate being red novae. In particular, V1309 Sco (a V838 Mon-class event) serves as one of the most promising examples of an active CE event (or merger) that is caught in action (Tylenda et al. 2011; Ivanova et al. 2013). V1309 Sco was the first stellar event to provide conclusive evidence that contact binary systems end their evolution in a stellar merger. The rate of red novae events has been estimated to be as high as 20% of the core collapse SN rate (Thompson et al. 2009). However, this 20% was computed without considering the difference between LRNe and ILRTs, which means that they were all considered to be the same type of objects. This value was therefore overestimated. A value of >5% was discussed in Botticella et al. (2009) when they presented SN 2008S.

Another promising example with a convincing link to a CE event is that of the LRN M31-2015-OT1, whose final progenitor binary system has been investigated (Williams et al. 2015; Lipunov et al. 2017; Blagorodnova et al. 2020) and simulated in detail (MacLeod et al. 2017). It has been suggested that this event, along with a number of other LRNe, might simply be more scaled-up versions of normal red novae (typically fainter than $M_V \sim -10$), thus resulting from merger events involving more massive stars than the less luminous red novae (Blagorodnova et al. 2017; Smith et al. 2016; Lipunov et al. 2017; Mauerhan et al. 2018; MacLeod et al. 2018; Pastorello et al. 2019a). There seems to be consensus in the literature for a direct link between the luminosities of various red novae phenomena and the masses of the stellar components undergoing coalescence (CE evolution). More specifically, the fainter red novae involve stellar masses of $\sim 1-5\,M_\odot$, such as V838 Mon and most likely have $5-10\,M_\odot$ components; whereas the LRNe stellar masses are thought to be a few $10\,M_\odot$ (Metzger & Pejcha 2017). In a recent population synthesis study, Howitt et al. (2019) reported a Galactic LRNe rate of $\sim 0.2\,\mathrm{yr}^{-1}$, in agreement with the observed rate. They also argued that the Large Synoptic
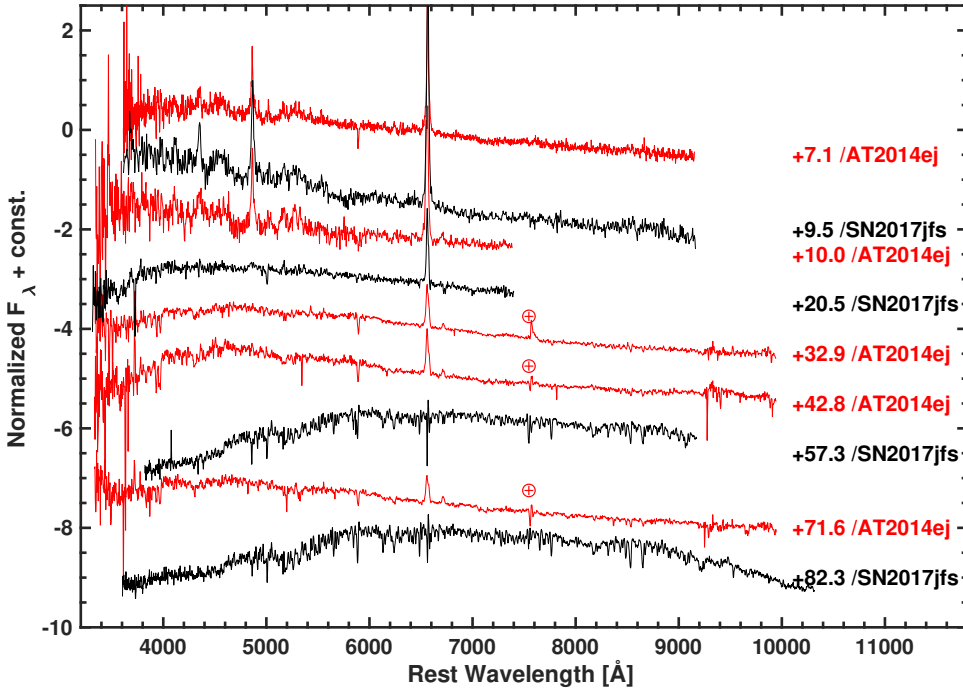
Fig. 11. Comparison of visual wavelength spectra of AT 2014ej with similar-epoch spectra of the LRN AT 2017jfs. Each of the spectra was corrected for reddening and is plotted in the rest-frame. Reported phases are in days relative to the first peak.

Survey Telescope will observe 20−750 LRNe per year. Such a rate will enable us to estimate the luminosity function of LRNe and reveal the diversity among CE events.

Pastorello et al. (2019a) provided a comprehensive review and discussion of the properties and progenitors of red novae and LRNe. The double-peaked light curves are still debated, but could be explained with a CE event by an initial ejected envelope, producing the low-luminosity light curve peak, followed by the merger of the secondary star onto the core component of the primary star. Metzger & Pejcha (2017) proposed that these double-peaked light curves arise from a collision between a dynamically ejected fast shell of material associated with the terminal stage of the CE merger with preexisting slow equatorial circumbinary material shed from the plunge-in of the secondary star during the early phase of in-spiral. In this scenario, the first optical peak arises through cooling envelope emission, and the second light-curve peak is powered by subsequent radiative shocks in the equatorial plane. Moreover, differences between various red gap transients might be explained by different viewing angles of observers with respect to the orbital plane of the progenitor binary (see Fig. 2 of Metzger & Pejcha 2017), along with several other key parameters characterizing the progenitor system.

Glebbeek et al. (2013) have studied the evolution of stellar mergers formed by a collision involving massive stars. They concluded that mass loss from the merger event is generally small (<10% of the total mass for equal-mass star mergers at the end of the main sequence) and that little hydrogen is mixed into the core of the merger product. This amount of mass loss may be sufficient to explain the double-peaked light curves in LRNe events, making this a viable model.

4.3. UVOIR light curves of luminous red novae

We plot in Fig. 13 the ultra-violet, optical, infrared (UVOIR) light curve of AT 2014ej, compared to those of our LRNe comparison sample. The overall morphology of the entire sample is similar, with all of the objects displaying a double-hump light curve typically of most LRNe. However, as previously noted by Pastorello et al. (2019a) and as shown in Fig. 13, there is diversity. This includes the luminosity of both peaks and the phase of the second peak relative to the first peak. Nevertheless, in general, there appears to be a correlation between the luminosity of the two peaks. In other words, objects whose first peak is located at the bright end of the luminosity distribution (i.e., AT 2017jfs, SNhunt248, NGC 4490-2011-OT, and AT 2014ej) also have secondary maxima at the bright end of the luminosity distribution. If this trend holds for a more populated sample, we might speculate that the luminosity of the second peak may scale with the masses of the involved ejecta and CSM undergoing circumstellar interaction.

We also plot in Fig. 13 the two closest matching light-curve models published by Metzger & Pejcha (2017) and discussed above. These include their fiducial model computed for a $10\,M_\odot$ system characterized with the semimajor axis $a = 30\,R_\odot$ and with a predynamical mass runaway time of $t_{run} = 10 \cdot t_{dyn}$, where t_{dyn} corresponds to the in-spiral dynamical timescale. The second synthetic light-curve model corresponds to the fiducial model with the mass increased to $30\,M_\odot$. This results in a brighter light curve relative to the fiducial model, but in general, the model fails to reach the luminosities exhibited at both peaks (by a factor of ∼10−15) for all but the faintest LRN M101-2015-OT1. In light of the differences in luminosity and the timescales describing the rise and decline of the second peak, it would be interesting to see the model calculations extended to even more massive systems, higher values of t_{run}, and even modifications to the assumed growth rate of predynamical mass loss.

5. Conclusion

In this study we have added observations to the growing populations of luminous red novae (LRNe). Our observational data set of AT 2014ej demonstrates characteristics of other LRNe, including the double-humped light-curve evolution that is ubiquitous to this class of red transients. These double-humped light curves are reminiscent of the long-lasting type IIn SN 2006jd,
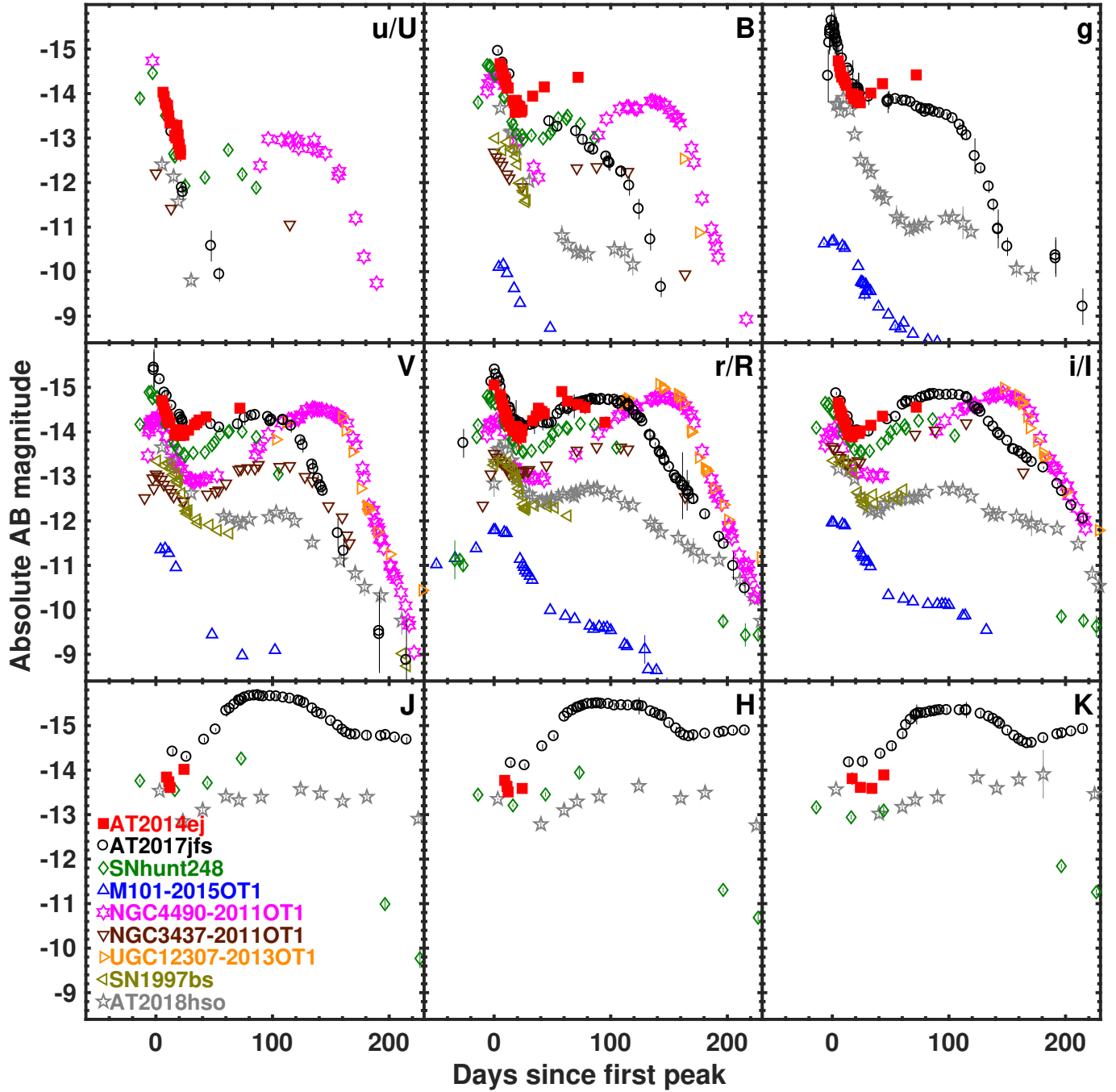
Fig. 12. Absolute magnitude light curves of AT 2014ej compared to other well-observed LRNe: SN 1997bs, NGC 3437-2011-OT1, NGC 4490-2011-OT1, UGC 12307-2013-OT1, M101-2015-OT1, SNhunt248, AT 2017jfs, and AT 2018hso. Each light curve is on the AB system.

which Stritzinger et al. (2012) argued to be produced by SN ejecta interacting with CSM located in a torus around the progenitor, and ejected during its pre-SN phase (Chugai & Danziger 1994). Similarly, Metzger & Pejcha (2017) attributed the second peaks observed in most LRN to material ejected following the CE merger of two massive stars that interacts with slow equatorial circumbinary material, previously ejected during the early phase of in-spiral. The Metzger & Pejcha (2017) models plotted in Fig. 13 exhibit a similar trend in their overall evolution to the trend in the LRN comparison sample. However, the models underpredict the luminosities of both peaks, and the timescales describing the evolution of the second peak differ.

Perhaps future efforts of modeling such systems should extend beyond the parameter space thus far considered.

To conclude, we wish to consider that less than a decade ago, our understanding of gap transients was significantly limited. In just a short time period, however, the landscape of gap transients has grown to be populated by various subtypes ranging from LBV eruptions to ILRTs possibly associated with electron capture supernovae, LRNe produced during the CE phase of massive binaries, and even to the faintest 2008ha-like SNe whose origins remain unknown. Efforts to further unravel the intricacies of gap transients will require detailed followup over long periods, while significant advancement in identifying the underlying
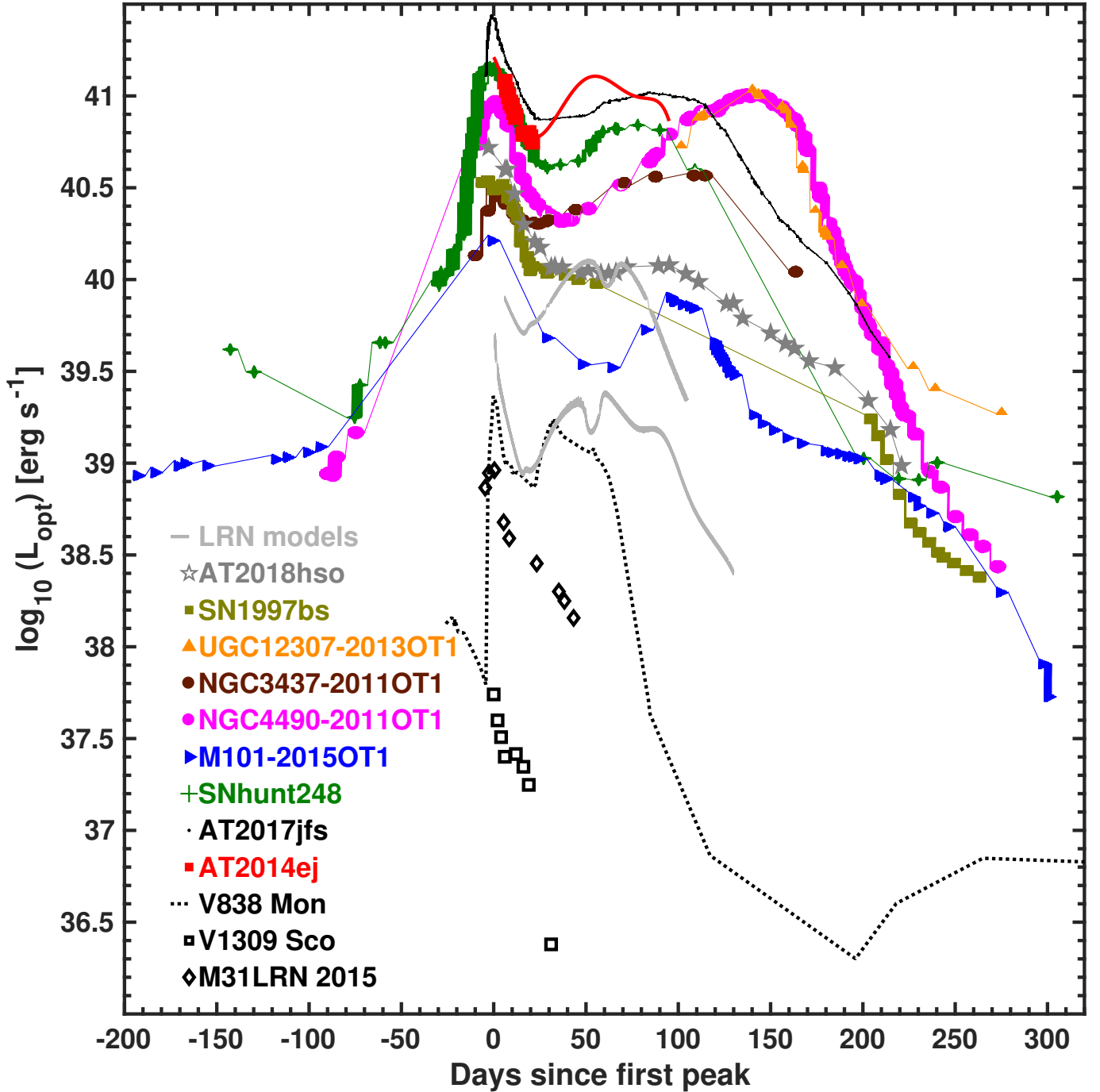
Fig. 13. Pseudo-bolometric light curves of a handful of well-observed LRNe from Tylenda (2005), Tylenda et al. (2011), Williams et al. (2015), Cai et al. (2019), and Pastorello et al. (2019a), plotted along with that of AT 2014ej. The solid red line extended beyond the UVOIR light curve of AT 2014ej corresponds to CHASE unfiltered photometry. Two LRN models published by Metzger & Pejcha (2017) are also overplotted as gray lines. This includes the light curve computed for their Y fiducial model assuming a binary mass of $10\,M_\odot$, a semimajor axis of $a = 30\,R_\odot$, and a predynamical mass runaway time of $t_{\mathrm{run}} = 10 \cdot t_{\mathrm{dyn}}$, as well as a second more luminous light curve produced from a model assuming a higher binary mass of $30\,M_\odot$.

progenitor populations of these objects can be expected with IR observations made with the *James Webb* Space Telescope.

References

Adams, S. M., Kochanek, C. S., Prieto, J. L., et al. 2016, MNRAS, 460, 1645

Bacon, R., Vernet, J., Borisova, E., et al. 2014, The Messenger, 157, 13

Bernstein, R., Shectman, S. A., Gunnels, S. M., Mochnacki, S., & Athey, A. E. 2003, in Instrument Design and Performance for Optical/Infrared Ground-based Telescopes, eds. M. Iye, & A. F. M. Moorwood, Proc. SPIE, 4841, 1694

Blagorodnova, N., Kotak, R., Polshaw, J., et al. 2017, ApJ, 834, 107

Blagorodnova, N., Karambelkar, V., Adams, S. M., et al. 2020, MNRAS, in press, [arXiv:2004.04757]

Bock, G., Marples, P., Parker, S., et al. 2014, Cent. Bur. Electron. Telegr., 3998, 1

Botticella, M. T., Pastorello, A., Smartt, S. J., et al. 2009, MNRAS, 398, 1041

Burns, C. R., Parent, E., Phillips, M. M., et al. 2018, ApJ, 869, 56

Cai, Y.-Z., Pastorello, A., Fraser, M., et al. 2019, A&A, 632, L6

Childress, M. J., Tucker, B. E., Yuan, F., et al. 2016, PASA, 33, e055

Chugai, N. N., & Danziger, I. J. 1994, MNRAS, 268, 173

Dahlem, M. 2005, A&A, 429, L5

Doherty, C. L., Gil-Pons, P., Siess, L., & Lattanzio, J. C. 2017, PASA, 34, e056

Filippenko, A. V. 1997, ARA&A, 35, 309

Fitzpatrick, E. L. 1999, PASP, 111, 63

Galbany, L., Anderson, J. P., Rosales-Ortega, F. F., et al. 2016, MNRAS, 455, 4087

Galbany, L., Anderson, J. P., Sánchez, S. F., et al. 2018, ApJ, 855, 107

Glebbeek, E., Gaburov, E., Portegies Zwart, S., & Pols, O. R. 2013, MNRAS, 434, 3497

Hashimoto, M., Iwamoto, K., & Nomoto, K. 1993, ApJ, 414, L105

Howitt, G., Stevenson, S., Vigna-Gómez, A. R., et al. 2019, MNRAS, 492, 3229

Humphreys, R. M., Bond, H. E., Bedin, L. R., et al. 2011, ApJ, 743, 118

Ivanova, N., Justham, S., Chen, X., et al. 2013, A&ARv, 21, 59

Kankare, E., Kotak, R., Pastorello, A., et al. 2015, A&A, 581, L4

Kashi, A., & Soker, N. 2016, Res. Astron. Astrophys., 16, 99

Kashi, A., Frankowski, A., & Soker, N. 2010, ApJ, 709, L11

Kiewe, M., Gal-Yam, A., Arcavi, I., et al. 2012, ApJ, 744, 10

Kitaura, F. S., Janka, H.-T., & Hillebrandt, W. 2006, A&A, 450, 345

Kochanek, C. S. 2011, ApJ, 741, 37

Kochanek, C. S., Szczygieł, D. M., & Stanek, K. Z. 2012a, ApJ, 758, 142

Kochanek, C. S., Khan, R., & Dai, X. 2012b, ApJ, 759, 20

Kulkarni, S., & Kasliwal, M. M. 2009, in Astrophysics with All-sky X-ray Observations, eds. N. Kawai, T. Mihara, M. Kohama, & M. Suzuki, 312

Lipunov, V. M., Blinnikov, S., Gorbovskoy, E., et al. 2017, MNRAS, 470, 2339

MacLeod, M., Macias, P., Ramirez-Ruiz, E., et al. 2017, ApJ, 835, 282

MacLeod, M., Ostriker, E. C., & Stone, J. M. 2018, ApJ, 863, 5

Mauerhan, J. C., Van Dyk, S. D., Johansson, J., et al. 2018, MNRAS, 473, 3765

Metzger, B. D., & Pejcha, O. 2017, MNRAS, 471, 3200

Meyer, F., & Meyer-Hofmeister, E. 1979, A&A, 78, 167

Miyaji, S., & Nomoto, K. 1987, ApJ, 318, 307

Miyaji, S., Nomoto, K., Yokoi, K., & Sugimoto, D. 1980, PASJ, 32, 303

Moorwood, A., Cuby, J. G., & Lidman, C. 1998, The Messenger, 91, 9

Morrell, N., Contreras, C., Gonzalez, C., et al. 2014, ATel, 6508, 1

Nomoto, K. 1984, ApJ, 277, 791

Nyholm, A., Sollerman, J., Tartaglia, L., et al. 2020, A&A, 637, A73

Osterbrock, D. E., & Ferland, G. J. 2006, Astrophysics of Gaseous Nebulae and Active Galactic Nuclei (Sausalito, CA: University Science Books)

Pastorello, A., & Fraser, M. 2019, Nat. Astron., 3, 676

Pastorello, A., Mason, E., Taubenberger, S., et al. 2019a, A&A, 630, A75

Pastorello, A., Chen, T. W., Cai, Y. Z., et al. 2019b, A&A, 625, L8

Persson, S. E., Murphy, D. C., Smee, S., et al. 2013, PASP, 125, 654

Pettini, M., & Pagel, B. E. J. 2004, MNRAS, 348, L59

Phillips, M. M., Simon, J. D., Morrell, N., et al. 2013, ApJ, 779, 38

Phillips, M. M., Contreras, C., Hsiao, E. Y., et al. 2019, PASP, 131, 014001

Pignata, G., Maza, J., Hamuy, M., Antezana, R., & Gonzales, L. 2009, Rev. Mex. Astron. Astrofis. Conf. Ser., 35, 317

Podsiadlowski, P. 2001, in Evolution of Binary and Multiple Star Systems, eds. P. Podsiadlowski, S. Rappaport, A. R. King, F. D'Antona, & L. Burderi, ASP Conf. Ser., 229, 239

Poelarends, A. J. T., Herwig, F., Langer, N., & Heger, A. 2008, ApJ, 675, 614

Prieto, J. L., Kistler, M. D., Thompson, T. A., et al. 2008, ApJ, 681, L9

Prieto, J. L., Sellgren, K., Thompson, T. A., & Kochanek, C. S. 2009, ApJ, 705, 1425

Reichart, D., Nysewander, M., Moran, J., et al. 2005, Nuovo Cim. C Geophys. Space Phys. C, 28, 767

Retter, A., & Marom, A. 2003, MNRAS, 345, L25

Schlafly, E. F., & Finkbeiner, D. P. 2011, ApJ, 737, 103

Schlegel, E. M. 1990, MNRAS, 244, 269

Smartt, S. J., Valenti, S., Fraser, M., et al. 2015, A&A, 579, A40

Smith, N., Ganeshalingam, M., Chornock, R., et al. 2009, ApJ, 697, L49

Smith, N., Li, W., Silverman, J. M., Ganeshalingam, M., & Filippenko, A. V. 2011, MNRAS, 415, 773

Smith, N., Andrews, J. E., Van Dyk, S. D., et al. 2016, MNRAS, 458, 950

Soker, N. 2020, ApJ, 893, 20

Soker, N., & Tylenda, R. 2003, ApJ, 582, L105

Stritzinger, M., Taddia, F., Fransson, C., et al. 2012, ApJ, 756, 173

Stritzinger, M., Taddia, F., Fraser, M., et al. 2020, A&A, 639, A103 (Paper I)

Taddia, F., Stritzinger, M. D., Sollerman, J., et al. 2013, A&A, 555, A10

Thompson, T. A., Prieto, J. L., Stanek, K. Z., et al. 2009, ApJ, 705, 1364

Tully, R. B., Courtois, H. M., Dolphin, A. E., et al. 2013, AJ, 146, 86

Tully, R. B., Courtois, H. M., & Sorce, J. G. 2016, AJ, 152, 50

Tylenda, R. 2005, A&A, 436, 1009

Tylenda, R., & Soker, N. 2006, A&A, 451, 223

Tylenda, R., Hajduk, M., Kamiński, T., et al. 2011, A&A, 528, A114

Van Dyk, S. D., Peng, C. Y., King, J. Y., et al. 2000, PASP, 112, 1532

Williams, S. C., Darnley, M. J., Bode, M. F., & Steele, I. A. 2015, ApJ, 805, L18

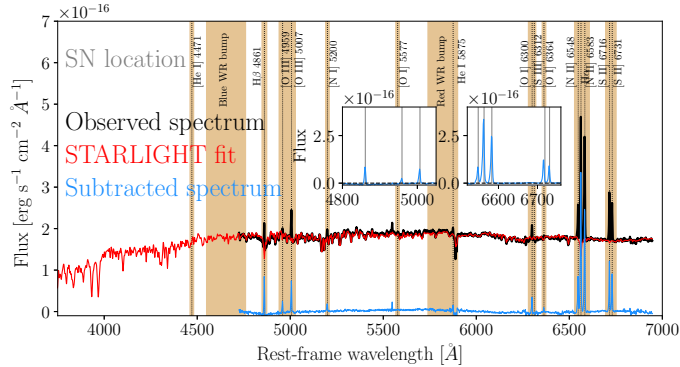## Appendix A: Metallicity and local environment

Fig. A.1. Visual wavelength MUSE spectrum at +390 d at the site of AT 2014ej in NGC 7552, shown in the host-galaxy rest frame and plotted in black. Prominent host nebular emission features are shown in blue and are labeled, and each fit with a single-Gaussian function after the background computed by STARLIGHT (red line) was subtracted. The nebular lines that are also shown in the insets provide flux ratios indicating a super-solar metallicity $(12 + \log(O/H) > 8.7 \pm 0.2 \, \mathrm{dex})$ on the O3N2 index at the location of AT 2014ej.

To study the properties of the environment of AT 2014ej, we used integral field spectroscopic observations of NGC 7552 taken with the European Southern Observatory's (ESO) Very Large Telescope (VLT) equipped with the instrument MUSE (Multi Unit Spectroscopic Explorer; Bacon et al. 2014) on 2015 October 11 that are available from the ESO Science Archive. The MUSE data set consist of a combination of three single pointings covering the same one squared arcmin field, with a total exposure of 3513 s. A one-dimensional extracted spectrum is plotted in Fig. A.1.

First, using a circular aperture of 2 arcsec diameter, we extracted a spectrum of the galaxy core and measured the six strongest gas-phase emission line features in the spectra to obtain an average redshift of $z = 0.00535 \pm 0.00003$, where the error is the mean error, which does not include the uncertainty related to the placement of the H II region in the galaxy. This is fully consistent with the value listed in the NED.

To estimate the local metallicity, we first extracted a circular spectrum with 2 arcsec diameter centered at the position of AT 2014ej and performed a similar analysis as described by Galbany et al. (2016, 2018). In summary, the spectrum was first fit with a modified version of STARLIGHT. The best-fit simple stellar populations (SSP) model was removed from the observed spectrum, which enabled us to obtain a pure gas-emission spectrum, Next the flux of the most prominent emission lines was estimated with Gaussian fits after correcting for dust attenuation. The adopted reddening value was derived from the Balmer decrement assuming case B recombination (Osterbrock & Ferland 2006) and a Fitzpatrick (1999) extinction law characterized by an $R_V = 3.1$.

From the extinction-corrected fluxes measured from Hα λ6563, Hβ λ4861, [O III] λ5007, and the [N II] λ6583 emission

lines, we obtain a measure of the oxygen metallicity abundance on the O3N2 index following the relation from Pettini & Pagel (2004). In doing so, a metallicity higher than solar of $12 + \log(O/H) = 8.7 \pm 0.2 \, \mathrm{dex}$ is inferred from the MUSE observations of NGC 7552 extracted at the position of AT 2014ej.

Appendix B: Galactic and host-galaxy reddening

The Milky Way reddening in the direction of AT 2014ej is very weak, with NED listing a Schlafly & Finkbeiner (2011) color excess $E(B-V)_{MW} = 0.012 \, \mathrm{mag}$, which, when a standard Galactic reddening law is adopted, corresponds to a visual extinction of $A_V^{MW} = 0.04 \, \mathrm{mag}$. Inspection of low- and medium-resolution spectra presented in Appendix A reveals conspicuous Na I D and also the K I $\lambda\lambda$7665,7699 interstellar lines located at the redshift of the host. Unfortunately, as demonstrated in Fig. B.1 (top panel), the Na I D lines are saturated in our higher dispersion spectrum and therefore do not provide a reliable estimate of the host reddening.

The K I lines in the MIKE spectrum that we show in Fig. B.1 (middle panel) can be used to estimate the host extinction. To estimate the host extinction from these features, we made use of Eq. (5) from Phillips et al. (2013), which connects the K I column density to the host visual-extinction A_V^{host}. Column density estimates were obtained with the Voigt profile-fitting program VPFIT[5]. The VPFIT fits to the data are shown Fig. B.1 and provide column density values of $\log_{10}(N_{Na I D}) = 12.09 \, \mathrm{cm}^{-2}$. Following Eq. (5) of Phillips et al. (2013), these values correspond to $A_V^{host} = 2.5 \pm 1.8 \, \mathrm{mag}$, where the accompanying uncertainties correspond to 72% of the inferred value of A_V^{host} (Phillips et al. 2013). This is a high extinction value with a high uncertainty. Therefore we resorted to estimating the reddening based on a relation between the strength of the diffuse interstellar band (DIB) at 5780 Å and A_V, again from Phillips et al. (2013).

Inspection of our medium-dispersion spectrum reveals the 5780 Å absorption feature (see Fig. B.1, bottom panel). We computed the equivalent width (EW) of the DIB feature by fitting a Gaussian function using the IRAF task fitprofs. In computing the fit, an FWHM value was set to 2.1 Å and the fitting range was set to be between 5778 and 5782 Å. The Gaussian fit provides an EW of 0.176 ± 0.020 Å, which, when Eq. (6) from Phillips et al. (2013) is used, implies $A_V^{host} = 0.92 \pm 0.47 \, \mathrm{mag}$. We verified that this value is fully consistent with the visual extinction of $A_V^{host} = 0.97 \pm 0.21 \, \mathrm{mag}$ implied by the Balmer decrement estimate from the MUSE spectrum presented in Appendix A that we plot in Fig. A.1. When we combine the DIB visual extinction estimate with the Milky Way contribution, we obtain a total visual extinction for AT 2014ej of $A_V^{tot} = 0.96 \pm 0.47 \, \mathrm{mag}$, which is adopted in this work. Moreover, to convert A_V^{tot} into extinction values appropriate for the different passbands we used to obtain photometry of AT 2014ej, we adopted a Fitzpatrick (1999) reddening law. We finally note that AT 2014ej might be associated with circumstellar dust, and therefore the assumed host-reddening value comes with the same caveats as discussed in Appendix B of Paper I (see also Kochanek et al. 2012b).
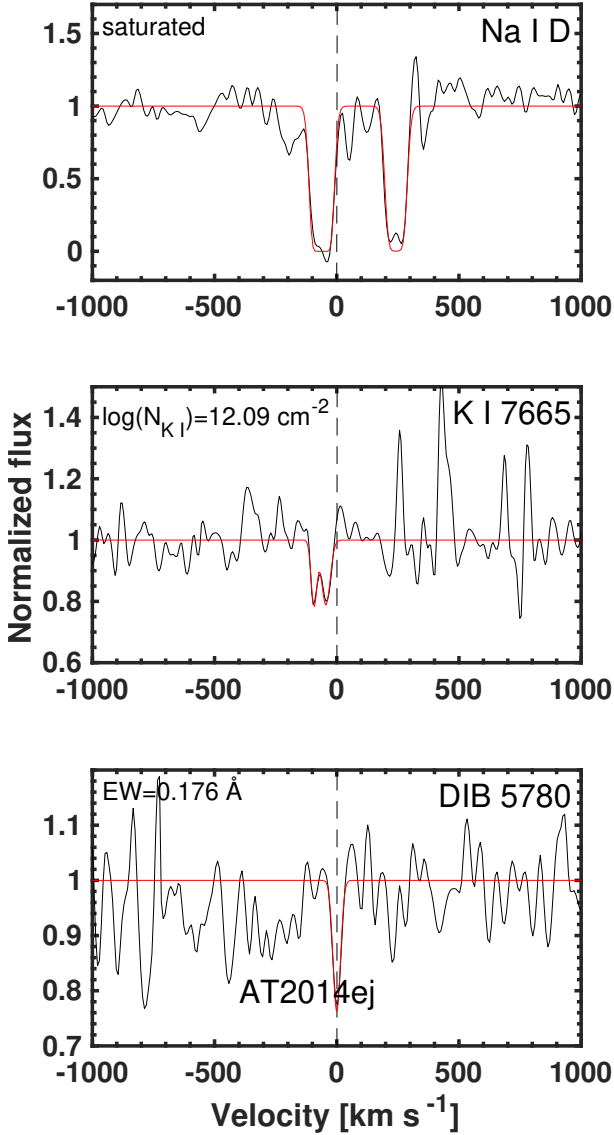
---

5   http://www.ast.cam.ac.uk/rfc/vpfit.html

Fig. B.1. VPFIT models (red line) for the (*top*) Na I D, (*middle*) K I, and (*bottom*) DIB at 5780 Å absorption features present in the *Magellan Clay* (+MIKE) medium-resolution spectrum (black line) of AT 2014ej discussed in detail in Appendix B. According to Phillips et al. (2013, see their Fig. 3), the column density for Na I D is at the saturation limit and therefore does not provide a reliable estimate for reddening. The K I lines do provide an extinction estimate, but come with a high uncertainty. Finally, according to Phillips et al. (2013, see their Eq. (6)), the EW of the DIB feature at 5780 Å estimated with fitprofs task in IRAF gives the visual extinction $A_V^{host} = 0.92 \pm 0.47$ mag. This value is fully consistent with the extinction value estimated using the Balmer decrement combined with line measurements made from the MUSE spectrum (see Fig. A.1) at the location of AT 2014ej.